Notch signaling and taxis mechanims regulate early stage angiogenesis: A mathematical and computational model

Short title: Notch signaling and taxis mechanims regulation of early stage angiogenesis

Rocío Vega[1], Manuel Carretero[1], Rui D.M. Travasso[2], Luis L. Bonilla[1,3*]

1 - G. Millán Institute for Fluid Dynamics, Nanoscience & Industrial Mathematics, and Department of Materials Science & Engineering and Chemical Engineering, Universidad Carlos III de Madrid, Avenida de la Universidad 30, 28911 Leganés, Spain
2 - CFisUC, Department of Physics, University of Coimbra, R. Larga, 3004-516 Coimbra, Portugal
3 - Courant Institute of Mathematical Sciences, New York University, 251 Mercer St, New York, N.Y. 10012, USA

* Corresponding Author

Abstract

During angiogenesis, new blood vessels sprout and grow from existing ones. This process plays a crucial role in organ development and repair, in wound healing and in numerous pathological processes such as cancer progression or diabetes. Here, we present a mathematical model of early stage angiogenesis that permits exploration of the relative importance of mechanical, chemical and cellular cues. Endothelial cells proliferate and move over an extracellular matrix by following external gradients of Vessel Endothelial Growth Factor, adhesion and stiffness, which are incorporated to a Cellular Potts model with a finite element description of elasticity. The dynamics of Notch signaling involving Delta-4 and Jagged-1 ligands determines tip cell selection and vessel branching. Through their production rates, competing Jagged-Notch and Delta-Notch dynamics determine the influence of lateral inhibition and lateral induction on the selection of cellular phenotypes, branching of blood vessels, anastomosis (fusion of blood vessels) and angiogenesis velocity. Anastomosis may be favored or impeded depending on the mechanical configuration of strain vectors in the ECM near tip cells. Numerical simulations demonstrate that increasing Jagged production results in pathological vasculatures with thinner and more abundant vessels, which can be compensated by augmenting the production of Delta ligands.

Author Summary

Angiogenesis is the process by which new blood vessels grow from existing ones. This process plays a crucial role in organ development, in wound healing and in numerous pathological processes such as cancer growth or in diabetes. Angiogenesis is a complex, multi-step and well regulated process where biochemistry and physics are intertwined. The process entails signaling in vessel cells being driven by both chemical and mechanical mechanisms that result in vascular cell movement, deformation and proliferation. Mathematical models have the ability to bring together these mechanisms in order to explore their relative relevance in vessel growth. Here, we present a mathematical model of early stage angiogenesis that is able to explore the role of biochemical signaling and tissue mechanics. We use this model to unravel the regulating role of Jagged, Notch and Delta dynamics in vascular cells. These membrane proteins have an important part in determining the leading cell in each neo-vascular sprout. Numerical simulations demonstrate that increasing Jagged production results in pathological vasculatures with thinner and more abundant vessels, which can be compensated by augmenting the production of Delta ligands.

Introduction

Angiogenesis is a process by which new blood vessels sprout and grow from existing ones. This ubiquitous phenomenon in health and disease of higher organisms [1], plays a crucial role in the natural processes of organ growth and repair [2],

wound healing [3], or inflammation [4]. Angiogenesis imbalance contributes to numerous malignant, inflammatory, ischaemic, infectious, and immune diseases [2, 5], such as cancer [6–10], rheumatoid arthritis [11], neovascular age-related macular degeneration [12], endometriosis [13, 14], and diabetes [15].

Either when a tissue is in hypoxia or during (chronic or non-chronic) inflammation, cells are able to activate signaling pathways that lead to the secretion of pro-angiogenic proteins. The Vascular Endothelial Growth Factor (VEGF) is one of these proteins and it is necessary and sufficient to trigger angiogenesis. Present in different isoforms, VEGF diffuses in the tissue, and is able to bind to extracellular matrix (ECM) components (its binding affinity is different for distinct VEGF isoforms), forming a well defined spatial concentration gradient in the direction of increasing hypoxia [16,17]. When the VEGF molecules reach an existing vessel, they promote the dwindling of the adhesion between vessel cells and the growth of newer vessel sprouts. VEGF also activates the tip cell phenotype in the vessel endothelial cells (ECs) [18]. The tip cells grow filopodia rich in VEGF receptors, pull the other ECs, open a pathway in the ECM, lead the new sprouts, and migrate in the direction of increasing VEGF concentration [19]. Branching of new sprouts occur as a result of crosstalk between neighboring ECs [20].

As the new sprouts grow, ECs have to alter their shape to form a lumen connected to the initial vessel that is capable of carrying blood [21–25]. Moreover, in order for the blood to be able to circulate inside the new vessels, the growing sprouts have to merge either with each other or with existing functional mature vessels [26]. The process by which sprouts meet and merge is called anastomosis [26–30].

Nascent sprouts are then covered by pericytes and smooth muscle cells, which provide strength and allow vessel perfusion. Poorly perfused vessels may become thinner and their ECs, in a process that inverts angiogenesis, may retract to neighboring vessels leading to more robust blood circulation [31, 32]. Thus, the vascular plexus remodels into a highly organized and hierarchical vascular network of larger vessels ramifying into smaller ones [33].

Therefore, angiogenesis is a multi-step, complex and well regulated process where biochemistry and physics are intertwined; with signaling in ECs being driven by both chemical and mechanical mechanisms that result in EC proliferation, mechanical deformation and cell movement.

In particular, the dynamical and biochemical processes that take place at the tip of every growing sprout are determinant for the growth, morphology and function of the resulting neo-vasculature. When an EC has the tip cell phenotype (which is triggered by the binding of VEGF to VEGF Receptor 2, VEGFR2) its membrane becomes rich in Delta-4 transmembrane proteins [20, 34]. These proteins bind the Notch transmembrane proteins in the neighboring cells triggering the Notch signaling pathway. The activation of this pathway down-regulates VEGFR2 and Delta-4, forcing the neighboring cells not to be in the tip cell phenotype, and to acquire the stalk cell phenotype [35]. Stalk ECs are characterized by a higher proliferation rate [19] triggered by both VEGF and by the tension exerted on them by the tip cell [36]. The sprouts are able to grow due to proliferation of the stalk ECs.

The ECs can interchange dynamically their phenotypes from tip to stalk. In fact, in the growing sprout the stalk ECs behind the tip cell are often able to overtake the tip cell and to take its place, thereby becoming tip cells and driving sprout elongation [37,38]. This dynamic behavior ensures that there is always a cell at the front of the sprout with the tip phenotype capable of exerting a contractile force on the matrix, degrading and remodelling matrix fibres and opening a pathway for the sprout to grow.

EC metabolism is strongly connected with this cycling dynamics at the tip of sprouts [39], and it is determinant to vascular patterning, pruning and sprouting [40–42]. The ability of ECs to rearrange themselves is essential for vessel remodelling [31]. Moreover, this dynamics at the tip is only possible due to the regulation of VE-cadherin expression in ECs by the Notch signaling pathway [37, 43, 44]. When the Notch-driven tip-stalk pattern is absent (due to very high VEGF levels, for example) the EC rearrangement dynamics stops [44]. In that case the vessels become thicker and sprouting is severely hampered. Hence, the Notch signaling pathway is pivotal in determining the morphology of blood vessel networks.

Importantly, the dynamics of the ECs' phenotypes in a growing sprout can be rather complex. While at moderate values of VEGF lateral inhibition by tip ECs can be observed [45], at higher VEGF concentrations the situation is different. Recently it has been experimentally observed that high levels of VEGF lead to synchronisation of phenotypes between cells at the sprout [46]. This phenomenon had first been suggested by theoretical models [18]. The model suggested that ECs in a sprout under high VEGF levels initiate acquiring the tip cell phenotype simultaneously, and then all simultaneously trigger the lateral inhibition by the Delta-Notch signaling, losing the tip phenotype and moving towards the stalk phenotype, only for the process to start again. Synchronised oscillatory behaviour in Delta-4 levels in EC cells has been observed under these conditions [46]. In this way, high VEGF hinders the

symmetry breaking needed for the lateral inhibition to take place in the sprout.

Recent mathematical models of Notch signaling in angiogenesis have also predicted states where the cells in the sprout are in a third intermediate state and neither in the tip nor in the stalk phenotype [47, 48]. The Jagged-1 transmembrane protein is an important partner in the regulation of the Notch signaling in angiogenesis, and its introduction in the computational models permit to predict these intermediate EC phenotypes [48–51].

Jagged-1 is a ligand of Notch and competes with Delta-4 in angiogenesis [52]. Experiments have shown that when the lateral inhibition pattern induced by Delta-Notch signaling is present, the levels of Jagged-1 follow the EC phenotype: they are lower in tip cells and higher in stalk cells (contrary to what happens with the levels of Delta-4) [53]. However, ECs are able to control independently the levels of Jagged-1 (for example by reaction with proteins of the Fringe family [52]), and therefore they are able to control the sensitivity to Notch-mediated lateral inhibition. Moreover, Jagged-1 also plays an important role in making the Notch mechanism capable of lateral induction, whereby a stalk EC may induce its neighbors to acquire a phenotype equal to its own [54]. For these motives, it is extremely important to understand the implications of Jagged-1 levels in sprouting angiogenesis. Mathematical models should integrate the knowledge of Delta-Notch-Jagged signaling with the dynamics of EC organization in a sprout to better understand how the communication between ECs in angiogenesis is mediated by Jagged-1.

Numerous mathematical models of angiogenesis study the growth of blood vessels and irrigation using continuum methods, cellular automata, and hybrid methods [36, 55–74]. Cellular Potts Models (CPM) [75, 76] of angiogenesis and vasculogenesis have been particularly successful in capturing vascular cell shape [77], vascular structure [66, 78] and in integrating the role of extra-cellular matrix (ECM) mechanics and structure [67, 79–81] in the development of the vasculature.

Many of these models use simplified models of the Notch pathway to determine the separation between sprouts [26, 68, 70]. However, very detailed models of the Notch signaling pathway that integrate the dynamics of filopodia growth and of anastomosis have been developed [18, 82]. These detailed models also shed light into the regulation of VE-Cadherin by Delta-Notch [37, 44] and into the coupling between EC metabolism, Delta-Notch and EC rearrangement dynamics at the tip [39].

Moreover, cell based mathematical models that include Jagged-1 and Fringe have been developed in the contexts of cell differentiation [49–51] and angiogenesis [48]. However, these models of sprouting angiogenesis use a fixed geometry of a linear array of cells, without taking into account that ECs in a sprout are elongated and have many neighbors, and that they move and proliferate. Therefore, to describe the regulating effect of Jagged-1 in the sprouting dynamics we need to integrate dynamical models that take into account Jagged-1 with a CPM that takes into account cell shape, movement and proliferation. In the present paper, we carry out this integration process for angiogenesis in the early stage, before sprouts form a lumen, become perfused and can regress. We use a CPM that incorporates cell motion following increasing gradients of VEGF (chemotaxis), of adhesion to substrate (haptotaxis) and of substrate stiffness (durotaxis), as well as a model of cell splitting and proliferation that uses an unsupervised machine learning algorithm, and the Notch signaling pathway. This model will permit to explore the relative importance of mechanical, chemical and cellular cues in angiogenesis.

The section Mathematical Model describes the CPM coupled with the Delta-Notch-Jagged dynamics. In the section Results and Discussion, we present the results of the simulation and how Jagged-1 determines sprouting dynamics. Finally, in the last section Conclusion we draw the conclusions of the manuscript.

Mathematical model

The mathematical model consists of a CPM in which the dynamics of the Notch signaling pathway in endothelial cells selects tip and stalk ECs. Tip ECs move by chemotaxis, haptotaxis and durotaxis and stalk cells proliferate. Vessel branching and anastomosis appear as a result of combined cell signaling, mechanical and chemical taxis.

Cellular Potts model

Square grid. We consider a square domain Ω of side L with grid points (x_i, y_j), where $x_i = i\,h$, $y_j = j\,h$ with $i, j = 0, \ldots, M-1$, $h = L/(M-1)$, and M is the number of nodes on a side of the square. The square contains $M \times M$ grid points and $(M-1)^2$ elementary squares (pixels), each having an area $L^2/(M-1)^2$. To enumerate

nodes, we use left-to-right, bottom-to-top order, starting from node 0 on the bottom left corner of the square and ending at node M^2-1 on the rightmost upper corner. In numerical simulations, we use $L = 0.495$ mm.

Objects, spins and Metropolis algorithm. Pixels $\mathbf{x}$ can belong to different objects Σ_σ, namely ECs, and ECM. The field (called spin in a Potts model) $\sigma(\mathbf{x})$ denotes the label of the object occupying pixel $\mathbf{x}$ [75]. Each given spin configuration for all the pixels in the domain has an associated energy $H(\{\sigma(\mathbf{x})\})$ to be specified below. At each Monte Carlo time step (MCTS) t, we select randomly a pixel $\mathbf{x}$, belonging to object Σ_σ, and propose to copy its spin $\sigma(\mathbf{x})$ to a neighboring (target) pixel $\mathbf{x}'$ that does not belong to $\Sigma_{\sigma(\mathbf{x})}$. The proposed change in the spin configuration (spin flip) changes the configuration energy by an amount $\triangle H|_{\sigma(\mathbf{x})\to\sigma(\mathbf{x}')}$, and it is accepted with probability (Metropolis algorithm) [67, 75]

$$P\left(\sigma(\mathbf{x})\to\sigma(\mathbf{x}')\right)(t) = \begin{cases} e^{-\Delta H|_{\sigma(\mathbf{x})\to\sigma(\mathbf{x}')}/T}, & \Delta H|_{\sigma(\mathbf{x})\to\sigma(\mathbf{x}')} > 0; \\ 1, & \Delta H|_{\sigma(\mathbf{x})\to\sigma(\mathbf{x}')} \leq 0. \end{cases} \tag{1}$$

The temperature $T > 0$ is measured in units of energy and it is related to an overall system motility. We have selected $T = 4$ in our simulations.

Energy functional. The energy functional H is

$$\begin{aligned} H &= \sum_{\Sigma_\sigma} \rho_{\text{area}} \left(\frac{a_\sigma - A_\sigma}{A_\sigma}\right)^2 + \sum_{\Sigma_\sigma} \rho_{\text{perimeter}} \left(\frac{p_\sigma - P_\sigma}{P_\sigma}\right)^2 + \sum_{\Sigma_\sigma} \rho_{\text{length}} \left(\frac{l_\sigma - L_\sigma}{L_\sigma}\right)^2 + \sum_{\mathbf{x},\mathbf{x}'\in\Omega'_{\mathbf{x}}} \rho_{\text{adh}}^{\tau,\tau'} \left(1-\delta_{\sigma,\sigma'}\right) \\ &+ H_{\text{durot}} + H_{\text{chem}}. \end{aligned} \tag{2}$$

Here the three first terms are sums over cells and the fourth one sums over all pixels. We have

- a_σ is the area of the cell Σ_σ, A_σ is the target area and ρ_{area} is the Potts parameter which regulates the fluctuations allowed around the target area. There are two cell types: non-proliferating tip and stalk cells with $A_\sigma = 78.50\,\mu\text{m}^2$ and proliferating cells with double target area, $A_\sigma = 157\,\mu\text{m}^2$. The target radius of a proliferating cell is $\sqrt{2}$ times that of a non-proliferating cell.

- p_σ is the perimeter of the cell Σ_σ, P_σ is the target perimeter and $\rho_{\text{perimeter}}$ is the Potts parameter which regulates the fluctuations allowed around the target perimeter. The target perimeters are $P_\sigma = 31.4\,\mu$m for non-proliferating cells, and thrice this, $P_\sigma = 94.2\,\mu$m, for proliferating cells.

- l_σ is the length of the cell Σ_σ, $L_\sigma = 49.5\,\mu$m is the target length of nonproliferating cells, $L_\sigma = 70\,\mu$m is the target length of proliferating cells, and ρ_{length} is the Potts parameter which regulates the fluctuations allowed around the target length. We define the length of the cell from the longest axis of an ellipse that has the same moment of inertia as the cell. The inertia tensor per unit cell area is [83]

$$I_{ij}(\sigma) = \frac{1}{N_\sigma} \sum_{\mathbf{X}\in\sigma} (|\mathbf{X}|^2\delta_{ij} - X_i X_j), \quad i,j = 1,2, \quad \mathbf{X} = \mathbf{x} - \frac{1}{N_\sigma}\sum_{\mathbf{y}\in\sigma}\mathbf{y}, \tag{3}$$

  where N_σ is the number of pixels in cell σ and the distances $\mathbf{X}$ in the inertia tensor are measured from the center of mass of the cell. Let us now consider an ellipse whose axes have lengths $2a$ and $2b$ ($a \geq b$). Its inertia tensor per unit area defined as in Eq. (3) has eigenvalues $b^2/4$ and $a^2/4$. Thus, a is twice the square root of the largest eigenvalue of the inertia tensor,

$$a = \sqrt{2\left[I_{11} + I_{22} + \sqrt{(I_{11}-I_{22})^2 + 4I_{12}^2}\right]}, \quad l_\sigma = 2\,a(\sigma). \tag{4}$$

  We define the length of the cell σ as $2a$, where a, given by Eq. (4), is calculated from the inertia tensor per unit area of Eq. (3). See also [84].

- The Potts parameter $\rho_{\text{adh}}^{\tau,\tau'} \geq 0$ is the contact cost between two neighboring pixels. The value of this cost depends on the type of the object to which the pixels belong (cell or medium). Since $\delta_{\sigma,\sigma'}$ is the Kronecker delta, pixels belonging to the same cell do not contribute a term to the adhesion energy.

- The net variation of the durotaxis term H_{durot} is [67]

$$\Delta H_{\text{durot}} = -\rho_{\text{durot}}\, g(\mathbf{x},\mathbf{x}') \left(h(E(\epsilon_1)) \left(\mathbf{v}_1 \cdot \frac{\mathbf{x}'-\mathbf{x}}{|\mathbf{x}'-\mathbf{x}|} \right)^2 + h(E(\epsilon_2)) \left(\mathbf{v}_2 \cdot \frac{\mathbf{x}'-\mathbf{x}}{|\mathbf{x}'-\mathbf{x}|} \right)^2 \right), \tag{5}$$

  where ρ_{durot} is a Potts parameter, $g(\mathbf{x},\mathbf{x}') = 1$ for extensions and $g(\mathbf{x},\mathbf{x}') = -1$ for retractions, ϵ_1 and ϵ_2 and $\mathbf{v}_1$ and $\mathbf{v}_2$ ($|\mathbf{v}_1| = |\mathbf{v}_2| = 1$) are the eigenvalues and eigenvectors of the strain tensor ϵ_T, respectively. They represent the principal strains and the strain orientation. ϵ_T is the strain in the target pixel for extensions, and the strain in the source pixel for retractions. $h(E) = 1/\left(1 + \exp\left(-\omega\left(E - E_\theta\right)\right)\right)$ is a sigmoid function with threshold stiffness E_θ and steepness ω. $E(\epsilon) = E_0\left(1 + (\epsilon/\epsilon_{\text{st}})1_{\epsilon\geq 0}\right)$ is a function of the principal strains, in which E_0 sets a base stiffness for the substrate, ϵ_{st} is a stiffening parameter and $1_{\epsilon\geq 0} = \{1,\ \epsilon \geq 0;\ 0, \epsilon < 0\}$: strain stiffening of the substrate only occurs for substrate extension ($\epsilon \geq 0$), whereas compression ($\epsilon < 0$) does not stiffen or soften the substrate. We have used the parameter values: $E_\theta = 15$ kPa, $E_0 = 10$ kPa, $\omega = 0.5$ kPa^{-1}, and $\epsilon_{\text{st}} = 0.1$ [67].

- The variation of the chemotaxis term H_{chem} is

$$\Delta H_{\text{chem}} = -\rho_{\text{chem}}(\mathbf{x},\mathbf{x}') \frac{1}{1+\alpha_{\text{chem}} C(\mathbf{x})} \left[C(\mathbf{x}') - C(\mathbf{x})\right], \tag{6}$$

  where $\rho_{\text{chem}}(\mathbf{x},\mathbf{x}') \geq 0$ is a Potts parameter that depends on the type of EC or ECM occupying pixels $\mathbf{x}$ and $\mathbf{x}'$ and will be specified later. Its magnitude is measured by a positive constant ρ_{chem}^0. We have $\alpha_{\text{chem}} = 0.3$ and C is the VEGF concentration in the corresponding pixel.

The values of the Potts parameters are listed in Table 1. They are chosen according to those proposed by Bauer *et al.* [77] and Van Oers *et al.* [67] and adjusted so as to make that every term of the net variation of the hamiltonian have the same order. The perimeter contribution, absent in Refs. [67, 77], is small compared to the other terms in Eq. (2), so that it only affects the computations in extreme cases (e.g., extremely thin cells, thin cells that stick to the blood vessel). We have added a factor in the chemotaxis term to regulate the fluctuation around the resting VEGF concentration. Note that if α_{chem} is equal to zero, we recuperate the original term of Bauer *et al.* [77]. The proposed value, $\alpha_{\text{chem}} = 0.3$, is small.

Parameter	ρ_{area}	$\rho_{\text{perimenter}}$	ρ_{length}	ρ_{durot}	ρ_{chem}^0	$\rho_{\text{adh}}^{\tau,\tau'}$ (cell-cell)	$\rho_{\text{adh}}^{\tau,\tau'}$ (cell-ECM)
Value	9000	250	7200	25	60000	8.25	16.50

Table 1. Dimensionless Potts parameters.

What is the effect of changing the numerical values of the Potts parameters? As previously stated, with the values in Table 1, every term of the net variation of the hamiltonian has the same order. Variations of 10% or smaller in Potts parameters do not change the outcome of the simulations. Variations larger than 10% with respect to those in Table 1 produce unrealistic effects, which are as follows.

- ρ_{area}. Larger increments force cells to reach their target area faster, thereby increasing cell proliferation. The corresponding term becomes more important than the chemotaxis mechanism, which produces slower evolution of vessels toward the hypoxic zone and large clumps of cells in the vessels. Large reductions of this Potts parameter produce irregular cell proliferation and a much larger variety of cell sizes.

- $\rho_{\text{perimenter}}$. Large increments produce round cells, whereas large reductions (up to $\rho_{\text{perimenter}} = 0$) create extremely long and narrow cells stuck to the vessel sprout due to the now dominant effect of the adhesion term.

- ρ_{length}. Large increments produce elongated cells and force them to reach their target length faster. The corresponding term becomes more important than the adhesion or area term. Then there appear isolated cells that take a long time to reach their target area and proliferate (if they are marked for proliferation). Large reductions (up to $\rho_{\text{length}} = 0$) produce rounder cells depending on the values of the other Potts parameters.

- ρ_{durot}. This parameter produces qualitative changes only if it is ten times larger than in Table 1. In such a case, durotaxis overwhelms chemotaxis and the perimeter penalty, leading to cells following the stiffness gradients and sticking to each other, which create very irregular vessels.

- ρ_{chem}. Larger increments make chemotaxis dominant. Then cells become bigger and elongated and sprouts extend more rapidly. Sometimes tip cells separate from their sprouts as chemotaxis dominates adhesion effects. Larger reductions produce rounder cells that do not polarize along a specific direction, and produce wider and slower sprouts.

- $\rho_{\text{adh}}^{\tau,\tau'}$. The adhesion Potts parameter take on different values for cell-cell and cell-ECM boundaries. If these values become equal (e.g., to 16.5), narrower sprouts are produced and there are cells that escape from them. Larger increments of cell-ECM adhesion, makes very costly for ECM to surround cells, which then stick to each other too much. Larger reductions of cell-ECM produces more elongated cells. Reducing cell-cell adhesion favors cells sticking to each other and acquiring irregular shapes since the zero energy for a pixel to be surrounded by other pixels of the same cell would be very similar to the small positive energy for the pixel to be surrounded by pixels of a different cell.

Continuum fields at the extracellular scale

VEGF concentration. The VEGF concentration obeys the following initial-boundary value problem [77]:

$$\frac{\partial C(x,y,t)}{\partial t} = D_f \left(\frac{\partial^2 C(x,y,t)}{\partial x^2} + \frac{\partial^2 C(x,y,t)}{\partial y^2} \right) - \nu\, C(x,y,t) - G(x,y,C),\ (x,y) \in \Omega,\ t > 0, \tag{7}$$

$$C(0,y,t) = 0,\ C(L,y,t) = S,\ C(x,0,t) = \frac{S}{L} x = C(x,L,t),\ (x,y) \in \partial\Omega,\ t > 0, \tag{8}$$

$$C(x,y,0) = 0,\ (x,y) \in \Omega. \tag{9}$$

In Eq. (7), the amount of VEGF bound by an EC per unit time is

$$G(x,y,C) = \begin{cases} \Gamma, & \text{if } \Gamma \leq \upsilon\, C(x,y) \text{ and } (x,y) \in \Sigma_{\text{EC}}, \\ \upsilon\, C, & \text{if } 0 \leq \upsilon\, C(x,y) < \Gamma \text{ and } (x,y) \in \Sigma_{\text{EC}}, \\ 0, & \text{if } (x,y) \notin \Sigma_{\text{EC}}, \end{cases} \tag{10}$$

where $\upsilon = 1\ \text{h}^{-1}$ and $\Gamma = 0.02\ \text{pg}/(\mu\text{m}^2\ \text{h})$ is the maximum amount of VEGF that it could be consumed by a cell per hour [63, 77]. Other values we use are $D_f = 0.036\ \text{mm}^2/\text{h}$, $\nu = 0.6498/\text{h}$ [77], and $S = 5 \times 10^{-19}\text{g}/\mu\text{m}^2$ (corresponding to 50 ng/mL [38, 85] for a sample having a 10 μm height [67]).

Strains. Following Ref. [67], we calculate the ECM strains by using the finite element method to solve the stationary Navier equations of linear elasticity:

$$\begin{aligned} K\ u &= f, \quad \text{in } \Omega, \\ u &= 0, \quad \text{in } \partial\Omega. \end{aligned} \tag{11}$$

Here K is the stiffness matrix, u is the array of the x and y displacements of all nodes and f is the array of the traction forces per unit substrate thickness exerted by the cells. For nodes outside ECs, $f = 0$. For nodes inside ECs, each component $f_k = \mu_{\text{force}} \sum_j d_{kj} \delta_{\sigma_k, \sigma'_j}$ represents the traction stress on the kth node, μ_{force}, times the sum of the distances, d_{kj}, between the kth node and any node j in the same cell (σ_k is the label of the cell at which node k belongs).

The global stiffness matrix K is assembled from the stiffness matrices K_e of each pixel,

$$K_e = \int_{\Omega_e} B^T D B\ d\Omega_e, \tag{12}$$

in which

$$D = \frac{E}{1-\nu^2}\begin{pmatrix} 1 & \nu & 0 \\ \nu & 1 & 0 \\ 0 & 0 & \frac{1}{2}(1-\nu) \end{pmatrix}, \tag{13}$$

and B is the strain-displacement matrix for a four-noded quadrilateral pixel (finite element) [67]. B is a 3×8 matrix that relates the 8-component node displacement u_e of each pixel to local strains ϵ,

$$\epsilon = Bu_e, \tag{14}$$

where $\epsilon = (\epsilon_{11}, \epsilon_{22}, \epsilon_{12})$ is the 3-component column notation of the strain tensor

$$\epsilon_T = \begin{pmatrix} \epsilon_{11} & \epsilon_{12} \\ \epsilon_{12} & \epsilon_{22} \end{pmatrix}. \tag{15}$$

We have used the numerical values $E = 10$ kPa, $\nu = 0.45$, and $\mu_{\text{force}} = 1$ N/m^2. With these definitions and the durotaxis term given by Eq. (5), ECs generate mechanical strains in the substrate, perceive a stiffening of the substate along the strain orientation, and extend preferentially on stiffer substrate. The simulated ECs spread out on stiff matrices, contract on soft matrices, and become elongated on matrices of intermediate stiffness [67].

Signaling processes

The Notch signaling pathway is activated when Notch (transmembrane receptor) belonging to a particular cell interacts with Delta-4 or Jagged-1 (transmembrane ligands) belonging to its neighboring cell (trans-activation), thereby releasing the Notch intracellular domain (NICD). NICD then enters the nucleus and modulates the expression of many target genes of the Notch pathway, including both the ligands Delta and Jagged. However, when Notch of a cell interacts with Delta or Jagged belonging to the same cell, no NICD is produced; rather, both the receptor (Notch) and ligand (Delta or Jagged) are degraded (cis-inhibition) and therefore the signaling is not activated. For a given cell i surrounded by other cells, the equations describing this pathway are [48]

$$\frac{dN_i}{dt} = r_N H^S(I_i, \lambda_{I,N}) - \{[k_C D_i + k_T D_{\text{ext}}(i)]\, H^S(I_i, \lambda_{D,F}) + [k_C J_i + k_T J_{\text{ext}}(i)]\, H^S(I_i, \lambda_{J,F}) + \gamma\}\, N_i, \tag{16}$$

$$\frac{dD_i}{dt} = r_D H^S(I_i, \lambda_{I,D}) H^S(V_i, \lambda_{V,D}) - \left[k_C N_i H^S(I_i, \lambda_{D,F}) + k_T N_{\text{ext}}(i) + \gamma\right] D_i, \tag{17}$$

$$\frac{dJ_i}{dt} = r_J H^S(I_i, \lambda_{I,J}) - \left[k_C N_i H^S(I_i, \lambda_{J,F}) + k_T N_{\text{ext}}(i) + \gamma\right] J_i, \tag{18}$$

$$\frac{dI_i}{dt} = k_T N_i \left[H^S(I_i, \lambda_{D,F}) D_{\text{ext}}(i) + H^S(I_i, \lambda_{J,F}) J_{\text{ext}}(i)\right] - \gamma_S I_i, \tag{19}$$

$$\frac{dV_{Ri}}{dt} = r_{VR} H^S(I_i, \lambda_{I,V_R}) - k_T V_{Ri} V_{\text{ext}}(i) - \gamma V_{Ri}, \tag{20}$$

$$\frac{dV_i}{dt} = k_T V_{Ri} V_{\text{ext}}(i) - \gamma_S V_i. \tag{21}$$

Here, N_i, D_i, and J_i are the number of Notch, Delta-4, and Jagged-1 proteins in the ith cell, respectively, at time t. I_i, V_{Ri} and V_i are the number of NICD, VEGF receptor and VEGF molecules, respectively, that are in the ith cell at time t. r_N, r_D, r_J, and r_{VR}, are the production rates of N, D, J, and V_R, respectively. The cis-inhibition and trans-activation rates are k_C and k_T, respectively, whereas γ and γ_S are degradation rates for N, D, J, V_R and for I, V, respectively. These parameters, their representative values and units are listed in Table 2. All unknowns in Eqs. (16)-(21) are initially zero but changing these initial conditions does not alter the outcome of simulations.

Parameter	r_N	r_D, r_J, r_{VR}	k_C	k_T	γ	γ_S
Value	1200	1000	5×10^{-4}	2.5×10^{-5}	0.1	0.5
Unit	molec/h	molec/h	(h molec)$^{-1}$	(h molec)$^{-1}$	h^{-1}	h^{-1}

Table 2. Rates appearing in Eqs. (16)-(21).

Outside the ith cell, the number of X molecules is

$$X_{\text{ext}}(i) = \frac{1}{P_i} \sum_{j \in \langle i \rangle} P_{i,j} X_j, \tag{22}$$

where $X = N, D, J$, and $j \in \langle i \rangle$ are the cells j sharing boundary of length $P_{i,j}$ with cell i. The perimeter of cell i, P_i, minus $\sum_{j \in \langle i \rangle} P_{i,j}$ is the length of its boundary that is not shared with any other cell. Note that $X_{\text{ext}}(i)$ is simply the sum of all X_j if the lengths $P_{i,j}$ are all equal and $P_i = \sum_{j \in \langle i \rangle} P_{i,j}$ because the whole boundary of cell i is shared with other cells. As the cell moves and its boundaries fluctuate due to cellular Potts dynamics, the membrane protein levels of the neighboring cells interacting with the moving cell also vary. In this way, the production rates of the different proteins in a cell are directly influenced by the interactions with its neighborhood and, in particular, by the membrane fluctuations of the cell. $V_{\text{ext}}(i)$ is the number of VEGF molecules outside the ith cell that interact with VEGF receptor cells to produce VEGF molecules inside the ith cell. The external VEGF cells come from the continuum field $C(x, y, t)$, which diffuses from $x = L$. Let $\mathbf{x}_i$ be the pixel of the ith cell that is closer to the hypoxic region. The number of external VEGF molecules in that pixel is $C(\mathbf{x}_i, t)$ multiplied by the conversion factor $\chi_V = N_A L^2/[(M-1)^2 M_V]$, where M_V is the molecular weight of the VEGF molecules and N_A is the Avogadro number. We have used $\chi_V = 1$, which is representative of VEGF molecules with a large molecular weight. In the numerical simulation, C is known in the grid points and its value at a pixel should be the average value of the four grid points of the pixel. Since these values are quite similar, we adopt the value of C at the bottom left grid point of the pixel $\mathbf{x}_i$ as $C(\mathbf{x}_i, t)$.

Parameter	$\lambda_{I,N}$, $\lambda_{V,D}$, $\lambda_{I,J}$	$\lambda_{I,D}$, λ_{I,V_R}	$\lambda_{D,F}$	$\lambda_{J,F}$	n_N, n_D, n_V, n_{V_R}	n_J	n_F	I_0, V_0	χ_V
Value	2.0	0.0	3.0	0.3	2.0	5.0	1.0	200	1.0

Table 3. Dimensionless parameters appearing in the Hill functions. I_0 and V_0 are activation numbers of NICD and VEGF molecules, respectively, and χ_V is the conversion factor.

The shifted, excitatory and inhibitory Hill functions appearing in Eqs. (16)-(21) are:

$$H^S(\xi, \lambda_{\eta,\zeta}) = H^-(\xi) + \lambda_{\eta,\zeta} H^+(\xi), \tag{23}$$

$$H^-(\xi) = \frac{1}{1 + \left(\frac{\xi}{\xi_0}\right)^{n_\zeta}}, \quad H^+(\xi) = 1 - H^-(\xi), \tag{24}$$

where H^S is excitatory for $\lambda_{\eta,\zeta} > 1$ and inhibitory for $\lambda_{\eta,\zeta} \leq 1$. In Eqs. (23)-(24), $\xi = V, I$, $\eta = I, V, D, J$, and $\zeta = N, D, J, V_R, F$ (the subscript F refers to Fringe, cf. [48]). The dimensionless parameters n_ζ and $\lambda_{\eta,\zeta}$ appearing in the Hill functions are listed in Table 3.

Variable	N_i, D_i, J_i, N_{ext}, D_{ext}, J_{ext}	I_i	V_{Ri}	V_i	V_{ext}	t
Scale	$\sqrt{r_D/k_C}$	$(k_T r_D)/(k_C \gamma_S)$	r_{V_R}/γ	V_0	$6V_0$	$1/\sqrt{k_C r_D}$
Value	$\sqrt{2} \times 10^3$	10^2	10^4	2×10^2	12×10^2	$\sqrt{2}$
Unit	molec	molec	molec	molec	molec	h

Table 4. Units for nondimensionalizing the Notch equations (16)-(21).

Cell types, proliferation, branching and anastomosis

Cell types. In the model, ECs may be on a tip, hybrid or stalk cell phenotype. In nature, tip cells are characterized by having high levels of Delta-4, VEGFR2, and active VEGF signaling (i.e., high levels of VEGF internalization). They develop filopodia and migrate along the VEGF-A gradient, leading the formation of new branches. Delta-4 proteins at tip cell membranes inhibit the neighboring cells (due to lateral inhibition) to adopt a tip phenotype, thereby forcing them to become stalk cells (with low Delta-4, VEGFR2 and internalized VEGF).

Likewise, in our model, tip cells are distinguished by the number of VEGF molecules they possess. Therefore, a cell that has V larger than all its neighbors and $V > 0.5 \max_i V_i(t)$ will acquire the tip cell phenotype and be very

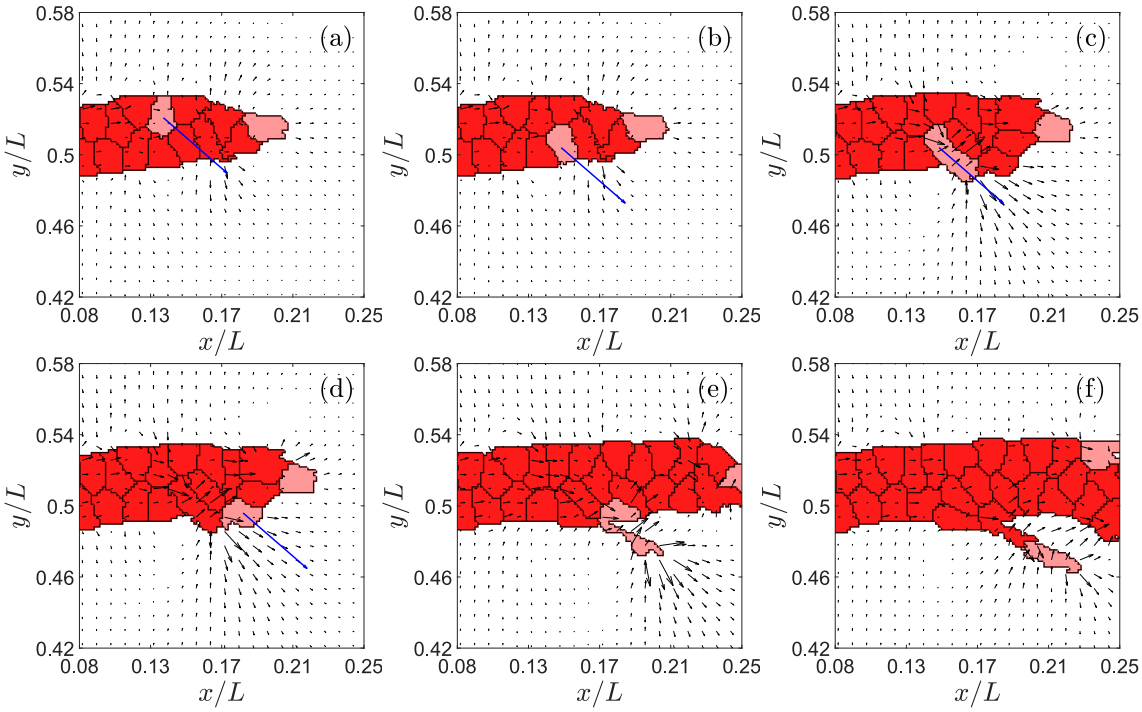

Figure 1. Example of tip cell exchange and branching in the direction of the blue arrow. Times in MCTS are: (a) 422, (b) 423, (c) 460, (d) 461, (e) 545, (f) 630. The black arrows in this figure represent the directions of largest eigenstrain and, therefore, they point to the likeliest direction of EC motion. The blue arrows indicate the actual direction of motion of a selected tip cell (marked in pink color) for the simulation we have carried out.

motile. To simulate this, tip cells are able to follow the mechanical and chemical cues on the environment, having $\rho_{\text{chem}} \neq 0$ and $\rho_{\text{durot}} \neq 0$. On the other hand, stalk cells are less motile. We consider two different cases: (A) nonmotile stalk cells with $\rho_{\text{chem}} = \rho_{\text{durot}} = 0$ in the model (except when they undergo proliferation, as explained below) [77]; and (B) motile stalk cells with the same ρ_{durot} as for the tip cells, but a smaller ρ_{chem} than that of the tip cells (see below). Stalk cells, by virtue of the lateral induction, characteristic of Notch-Jagged signaling, are able to induce neighboring cells to adopt a stalk cell phenotype, by promoting a decrease of internal VEGF in them.

In our model we track the cells belonging to each growing vessel. A new sprouting vessel can be formed when a stalk cell acquires the tip phenotype. This cell can then become the leading cell of a new vessel that branches out from out the old one. This is illustrated in Fig. 1. If the levels of VEGF inside the tip cells that lead an active growing branch drop to values in the interval $0.2\ \max_i V_i(t) < V < 0.5\ \max_i V_i(t)$, these cells will be in the hybrid phenotype. In spite of the lower amount of Delta-4, VEGFR2 and VEGF, these cells remain with the tip cell characteristics and are able to lead the sprout. Similarly, stalk cells whose internal VEGF increases to the same range acquire the hybrid phenotype and can lead a sprout. The number of cells in the hybrid phenotype is only appreciable for larger Jagged production rates.

Branching. When a stalk cell acquires the tip cell or the hybrid tip/stalk cell phenotype, this event will lead to the creation of a new active sprouting branch depending on its localization within the existing branch and on its moving direction.

To create a new branch, the boundary of the tip cell must touch the ECM. Moreover, let $\mathcal{P}$ be the set of $n_{\mathcal{P}}$ ECM pixels that have boundary with the branching tip cell. For each pixel $\mathbf{x}_p \in \mathcal{P}$, let the *strain vector* be $\mathbf{v}_p = \epsilon_j \mathbf{v}_j$, where ϵ_j is the largest eigenstrain at pixel $\mathbf{x}_p$ and $\mathbf{v}_j$ is the corresponding unit eigenvector, as defined after Eq. (5). The average modulus and argument for the branching cell i are

$$\Lambda_i = \frac{1}{n_{\mathcal{P}}} \sum_{p \in \mathcal{P}} |\mathbf{v}_p|, \quad \theta_i = \frac{1}{n_{\mathcal{P}}} \sum_{p \in \mathcal{P}} \text{Arg}\ \mathbf{v}_p. \tag{25}$$

Let us also assume that the gradient of the chemotactic factor C forms an angle Θ with the x-axis. The new tip cell will branch out, creating a new vessel, if the direction given by θ_i points in the direction of the ECM and if $-\pi/2 < \theta_i - \Theta < \pi/2$. For other values of θ_i, the tip cell does not leaves the parent vessel, since the chemotactic term of Eq. (6) opposes branching. In those cases, the direction given by θ_i points to another cell, not to the ECM. To facilitate branching computationally, we directly exchange the new tip cell with this neighboring cell (see Figs. 1(a) and 1(b)). These exchanges may continue in successive MCTS until the new tip cell reaches a boundary of the blood vessel for which the direction given by θ_i points to the ECM, as shown in Fig. 1. These cell exchanges in 2D mimic the climbing motion of the new tip cell over the parent vessel in a 3D geometry without merging with it.

We set the branching process to take at least 400 MCTS (incubation time). During this time we implement a persistent motion of the new tip cell in the direction marked by the angle θ_i. During this incubation period, and to provide a good separation from the parent vessel we permit the tip cell to proliferate once (see Figs. 1(e) and 1(f), and see below). After this time, the dynamics of the branching vessel follows the same rules as that of any other actively sprouting vessel.

Cell proliferation and duration of one MCTS. Endothelial cell proliferation in sprouting angiogenesis is regulated by both mechanical tension and VEGF concentration. In sprouting angiogenesis the tip cell creates tension in the cells that follow its lead. On those first stalk cells, this tension produces strain that triggers cell proliferation, if VEGF concentration is high enough [36]. Therefore, in our model, for each active sprouting vessel, one of the stalk cells that is in contact with a tip cell is randomly chosen to undergo proliferation. Only one cell per sprout proliferates. Tip cells in the model cannot proliferate, except only once when they start a new branch. Once a stalk cell attached to a tip cell has been randomly selected as a proliferating cell, its target area in the CPM is set to become twice the size, whereas its target perimeter is set to a value three times that of non-proliferating cells. This cell will then grow in successive MCTS until it reaches this large target area. Then the cell proliferates if the following three conditions hold: (i) $C(\mathbf{x}_i, t) > \psi_p$ (external VEGF surpasses a threshold), (ii) the cell belongs to an active blood vessel with cell proliferation, and (iii) the cell is not surrounded completely by other cells. Failure to meet one of these conditions precludes proliferation. If the three conditions are met, we use the unsupervised machine learning algorithm *K-means clustering* to split the cell. This algorithm calculates the Euclidean distance of each pixel in the cell to the centroid of two groups of pixels and corrects the centroids until the two pixel groups are balanced. These two groups comprise the new cells. Provided the daughter cells share boundary with the tip cell, one of them is randomly chosen to retain the ability to proliferate but the other cell does not proliferate. If the daughter cells do not share boundary with the tip cell, they both become non-proliferating and a different cell that shares boundary with the tip cell is randomly chosen to become a proliferating cell.

The actual proliferation rate depends on the duration of the cell cycle in MCTS and on how many seconds one MCTS lasts. The latter time is fitted so that numerical simulations reproduce the experimentally observed velocity of a sprouting vessel. We consider two cases. In case (A), we drop the elongation constraint $\rho_{\text{length}} = 0$ and make the stalk cells insensitive to chemo and durotaxis, therefore $\rho_{\text{chem}} = \rho_{\text{durot}} = 0$ for them. Only tip cells move in this case. In case (B), stalk cells also move, albeit more slowly than tip cells. While $\rho_{\text{durot}} = 25$ for both types of EC, $\rho_{\text{chem}}(\mathbf{x}, \mathbf{x}')$ is given by

$$\rho_{\text{chem}}(\mathbf{x}, \mathbf{x}') = \frac{\rho^0_{\text{chem}}}{\max_k D_k} \begin{cases} D_i, & \mathbf{x} \in \Sigma_i,\ \mathbf{x}' \in \Sigma_{\text{ECM}} \text{ or vice versa,} \\ \frac{D_i + D_j}{2}, & \mathbf{x} \in \Sigma_i,\ \mathbf{x}' \in \Sigma_j \text{ or vice versa,} \end{cases} \tag{26}$$

where i and j are ECs. The level of Delta-4 determines the EC phenotype and, according to Eqs. (6) and (26), the strength of their chemotactic drive. Tip cells have a higher level of Delta-4 and, consequently, they are more motile than stalk cells. As the latter also move, it may occur, as shown in Fig. 2, that a stalk cell overtakes a tip cell to become the leading cell of its sprout. This has been observed in experiments [37, 38] and in numerical simulations of CPMs different from ours [86]. In our model, the imposed strong gradient of the VEGF concentration $C(\mathbf{x}, t)$ precludes ECs to reverse their direction, unlike the CPMs in Ref. [86], which set a constant external VEGF concentration for their simpler Notch-Delta signaling dynamics. In Ref. [86], chemotaxis is guided by the gradients of a chemical signal secreted by the ECs (seemingly different from VEGF). The chemical signal also diffuses and is consumed by the ECM. Local chemical signal gradients may become contrary to the motion of a given EC, thereby facilitating reversal of its motion. In our model on the other hand, numerical simulations show that a growing sprout

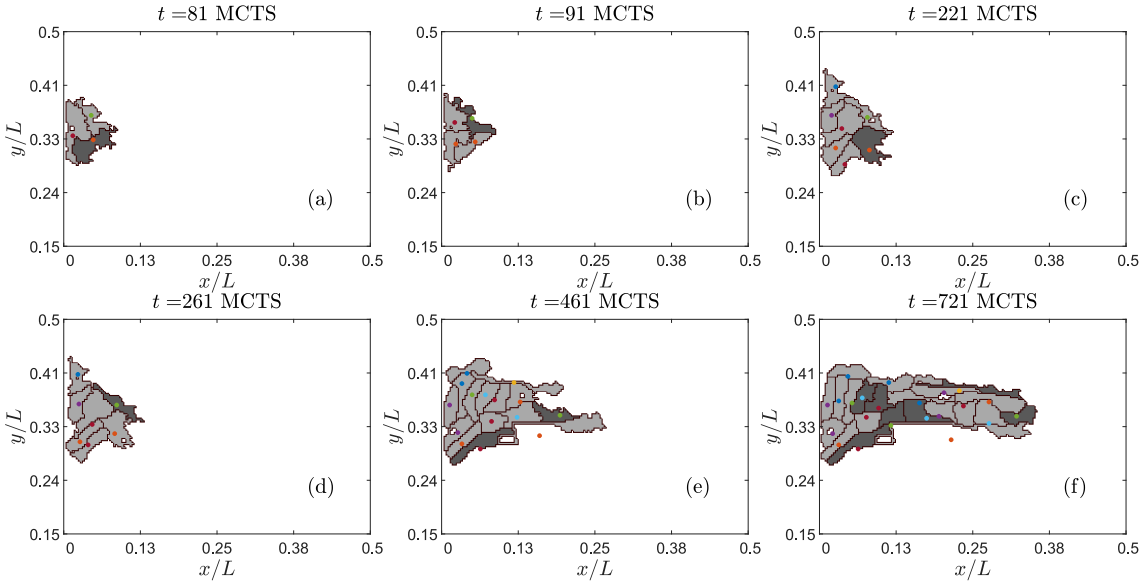

Figure 2. Examples of stalk cells (light color) overtaking tip cells (dark color) in numerical simulations with case (B) dynamics. EC centers are marked by dots. Note that ECs are more elongated than those undergoing case (A) dynamics.

may separate from the primary blood vessel more than one cell diameter (10 μm). As the primary vessel is a source of ECs, we create a new stalk cell to fill the resulting hole if this happens.

To obtain the equivalence between the number of MCTS and the time measured in experiments, we measured the pixel size in Fig. 1H of Ref [85], which is 0.9 μm. According to Fig. 3C of the same reference, the vessel mean elongation is 150 pixels (135 μm) in 36 hours for 50 ng/mL VEGF concentration. In our simulations of case (A) dynamics, the vessel mean elongation is 495 μm in 3001 MCTS. Thus, we set 1 MCTS to be 0.044 hours. A similar calculation for case (B) dynamics yields 1 MCTS = 0.03 hours (vessel mean elongation of 247.5 μm in 2200 MCTS).

We can estimate roughly EC proliferation time by dividing the MCTS one sprout is active by the number of cells created in the sprout during that time. We discard those sprouts whose ECs have never proliferated and average over all numerical simulations with the same dynamics, i.e., cases (A) and (B). The resulting proliferation times are 120 MCTS (5.28 hours) for case (A), and 217 MCTS (6.51 hours) for case (B). The proliferation times thus obtained are lower bounds: although only one EC of a given sprout is selected to proliferate at a given time, we cannot guarantee that the same EC of the same sprout will proliferate again at a later time. It could be a different cell that proliferates next, which would surely occurs when performing different numerical simulations. Then the average time for one EC to complete its cell cycle should be longer than that given by our estimation. With this proviso, our proliferation times are shorter but of the same order of magnitude as previously reported division times for EC in vivo or in vitro (83 minutes for cell mitosis but 17.8 hours to complete the cell cycle [87]). Fine tuning of parameters and better estimations of the cell cycle from numerical simulations might produce better agreement with reported experimental values, which, anyway, present some variability.

Anastomosis. When an active sprouting blood vessel merges with another active sprouting vessel, i.e. during anastomosis, one of them becomes inactive. If the collision occurs between tip cells of two different vessels, one vessel is randomly chosen to become inactive. If one tip cell merges with a stalk cell of a different active sprouting vessel, the vessel to which the tip cell belongs becomes inactive. The cells of an inactive vessel do not proliferate or branch, although they continue to undergo Notch signaling dynamics.

Results and discussion

The simulations of our model were implemented on Graphics Processing Units (GPU) using C-CUDA (CUDA: Compute Unified Device Architecture created by NVIDIA Corporation). This software contains source code provided by NVIDIA Corporation. The visualization of the results uses Matlab. We have elaborated our own simulation code, which is based on that by van Oers *et al.* [67] (implemented in the programming language C with Matlab visualization), K-means CUDA algorithm [88], standard algorithms (Euler, finite differences and finite elements) to solve ordinary and partial differential equations and CUDA libraries that are specified in the Supplementary Material. The flow diagram of the model is presented in Fig. 3, which encompasses the different computational modules for branching, cell proliferation, VEGF concentration, cell signaling processes, mechanics, CPM and anastomosis, cf the Supplementary Material. Due to the complexity of the model, parallel computing using C-CUDA allows the reduction of the computational times as much as possible. The amount of processes that can be calculated at the same time (over pixels, cells, vessels...) make this problem manageable. Furthermore, the implementation of our own code allow us to control times, features, parallel processes and the addition or changes of modules. The computation time of each reported simulation in a computer with Intel(R) Core(TM) i7-7700K CPU @4.20 GHz processor, 64.0 GB RAM and NVIDIA GeForce GTX 1080 graphics card is about 4 hours. We have run our simulation models for a simple slab geometry and different conditions. A primary vessel is supposed to be along the y axis. The initial VEGF concentration $C(\mathbf{x}, 0)$ is independent of y and decays linearly in x from $x = L$ to $x = 0$. Thus, chemotaxis pushes tip cells towards the vertical line at $x = L$. Most of the results we present below are illustrated with simulations of case (A) dynamics. Except for obtaining more elongated cells and allowing for stalk cell overtaking tip cells, case (B) dynamics produces qualitatively analogous results, as we comment where appropriate.

Cellular mechanics and anastomosis. It is clear that without the deformation of ECM induced by cells tractions and the strain vectors, there will be no branching direction for new tip cells to exit from a given sprout. Thus, cellular mechanics is crucial for branching. We have also found that cellular mechanics significantly controls anastomosis. The arrows in Fig. 4 are directed along the strain vector (eigenvector corresponding to the largest eigenstrain and having length equal to that eigenstrain). According to Eq. (5), the arrows indicate the likeliest direction in which ECs will move. The snapshots depicted in Fig. 4 show examples of successful and frustrated anastomosis and branching of advancing blood vessels. A tip cell leads successful branching from the blood vessel at the bottom of Fig. 4(a), as shown by Panels (b) and (c). Meanwhile, two blood vessels that sprout from the blood vessel at the top of Fig. 4(a) successfully anastomose as shown in Fig. 4(c). Notice that the strain vectors show the path of the approaching vessels until they anastomose. However, the branches arising from the two lowest vessels in Fig. 4(a) do not anastomose. They approach each other in Fig. 4(c) but the strain vectors pull them away from each other and anastomosis is frustrated, as shown in Figs. 4(d) and 4(e) [67, 89, 90].

Tip cells have higher levels of VEGF and their motion follows stiffness, chemical and adhesion gradients, as expected from the model. In successful anastomosis, one tip cell is directed by the strain vector to one actively sprouting vessel. When it makes contact, it fuses with that vessel. After that, the VEGF in the tip cell decreases and it becomes a stalk cell.

Jagged–Delta dynamics and sprouting. Jagged and Delta dynamics determine sprouting [48, 49]. Studies of Notch signaling in one cell driven by external Jagged and Delta molecules show that the phenotype of a tip cell changes to hybrid tip/stalk and then to stalk cell as the external Delta concentration surpasses successive thresholds (cf. Fig. 3 of Ref. [48]). The thresholds depend on the Jagged production rate. Lateral induction works similarly for one cell driven by external Jagged molecules: tip cells change to hybrid tip/stalk and stalk phenotypes as the external Jagged concentration surpasses successive Delta-dependent thresholds [48, 49]. Simulations of our model illustrate the effects of J-N and D-N signaling combined with chemo-, hapto- and durotaxis. Figure 5 shows that increasing the Jagged production rate r_J yields smaller branching blood vessels, thereby decreasing the irrigation of the hypoxic region. Furthermore, sprouting is accelerated as the Jagged production augments: thinner and less efficient sprouts are formed faster as r_J increases. Stalk cells proliferate on advancing sprouts. Thus, increasing the number of tip cells leading sprouts results in increasing cell proliferation and a more rapid sprout advance. This behavior conforms with the sketch in Fig. 5A of Ref. [48], which indicates that pathological angiogenesis is obtained when there is an excess Jagged production. The sprouts in physiological angiogenesis are thicker and advance more

slowly than the more abundant and thinner sprouts in pathological angiogenesis, as shown in Fig. 5.

The Delta production rate r_D acts opposite to r_J. High and intermediate levels of r_D ensure physiological angiogenesis, whereas the numbers of the hybrid tip/stalk cells increase for low levels of r_D. In more detail, we observe that, for $r_J = 500$ molec/h and $r_D = 1000$ molec/h, Figs. 6(a) and 6(b) show a gap between the VEGF of stalk and tip cells: the content of V is very low for stalk cells. It increases monotonically with V_{ext} and J for hybrid-tip and tip cells. Fig. 6(b) also shows that tip cells and hybrid tip-stalk cells have larger J than stalk cells. As r_J increases, at $r_J = 2000$ molec/h, the hybrid-tip cells have proliferated and bridge the gap in V, as depicted in Figs. 6(c) and 6(d). Fig. 6(d) indicates that J is smaller for the tip cells at large Jagged production rates, which is consistent with lateral induction of stalk phenotype by stalk cells with large J values [48]. For large r_J, tip cells have less Jagged ($J \approx 10$ and $V > 2$) than other cell types (J between 10 and 15 and $V < 2$), as shown in Fig. 6(d). Fig. 6(e) and 6(f) show that the Delta production rate r_D acts in opposition to r_J. At $r_D = 7500$ molec/h, Fig. 6(e), there is again a gap between the VEGF of stalk and tip cells. At this large Jagged production rate, tip cells have lower Jagged than stalk cells, as depicted in Fig. 6(f), which is similar to Fig. 6(d). However, Fig. 6(f) exhibits a gap between the maximum value of J for tip cells and the values of J for stalk cells, as compared to Fig. 6(d).

Jagged–Delta dynamics and anastomosis. What is the effect of modifying J-N and D-N signaling on angiogenesis? Figs. 5 and 7 show the effects of lateral inhibition by D-N signaling versus lateral induction by J-N signaling. Increasing the Jagged production rate produces more hybrid tip/stalk cells and more sprouts, as shown by Figs. 5 and, for the higher content of hybrid tip/stalk cells, by Figs. 6(c) and 6(d). However, for a high Jagged production rate, increasing the Delta production rate favors lateral inhibition by tip cells, which eventually decreases the number of new sprouts, makes anastomosis less frequent, as illustrated by Figs. 5(g), 5(h), 5(i), and 7.

Fig. 8 shows the concentrations of N, V, J and D for a developed angiogenic network for several values of the Jagged-1 and Delta-4 production rates. We observe that tip cells have large values of V and D for both normal ($r_J = 500$ molec/h) and high ($r_J = 2000$ molec/h) Jagged production rates, cf. Figs. 8(g)-(i) and 8(m)-(o). These figures highlight the role of lateral inhibition on stalk cells that are neighbors of tip cells. For large r_J, Figs. 8(k) and 8(l) show that stalk cells clearly have larger values of J, thereby illustrating the more important role of lateral induction. For large r_J and moderate r_D, Fig. 8(h) exhibits a larger number of cells with intermediate values of their internal VEGF, which shows the abundance of the hybrid tip/stalk cell phenotype. This is not the case for lower Jagged production rate as shown by the VEGF content in Figs. 8(g) and, for higher Delta production rate, in Fig. 8(i). As explained before and as shown by comparing Figs. 6(b) to 6(d) and 6(f), stalk cells have a smaller value of J than tip or hybrid tip/stalk cells at smaller Jagged production rates. In these cases, lateral inhibition by D-N signaling is more important. Figs. 8(m), 8(n) and 8(o) show that the D level of stalk cells is much reduced as compared with that of neighboring tip cells. Increasing the production rate of Delta-4 restores the morphology of the advancing normal vasculature to angiogenesis with high Jagged production rate, as shown by a comparison of Fig. 8(n) to Figs. 8(o) and 8(m).

Figure 9 further shows the effect of varying the production rates of Jagged and Delta on the advance and morphology of the vascular plexus. With respect to the simulations in Figs. 1 and 4 for standard values of r_J and r_D, increasing the production of Jagged, as shown in Fig. 5, produces more tip cells that run faster, cf. Figs. 9(a) and 9(b). Thus, lateral induction mediated by Jagged accelerates the advance of vasculature and increases the number of blood vessels by creating more hybrid tip/stalk cells, as explained before in relation to Figs. 5 and 6. If we keep constant r_J and increase the Delta production rate, lateral inhibition by tip cells becomes stronger, cf. Fig. 5. Then the number of tip cells decreases whereas the vasculature advances only slightly faster because angiogenesis and anastomosis diminish compared with the case of smaller r_D, cf. Fig. 9(c) and 9(d).

Sensitivity. The sensitivity of the results to the particular parameter set chosen is studied by varying one parameter at a time. In previous paragraphs, we have analyzed the effect of varying Potts parameters on the simulations of the model. They affect the relative importance of mechanical and chemical cues as described, and their effects are consistent with previous works on chemotaxis [77] and durotaxis [67]. Here we discuss the sensitivity of simulation results to changes in the parameters controlling cellular signaling. To this end, we have carried out 6 simulations for each of the production rates mentioned above and taken the averages of these realizations. Figs. 10(a) and 10(b) display, as a function of time, the number of angiogenic sprouts and the percentage of pixels of the hypoxic region at $x = L$ that are occupied by them, respectively. The number of sprouts and the occupation fraction ϕ should

be contrasted with Figs. 5 to 7. For fixed $r_D = 1000$ molec/h, increasing r_J produces thinner and more numerous pathological sprouts that arrive faster to $x = L$. Increasing r_D at a higher r_J decreases the proliferation of sprouts and the fraction of pixels occupied by them at the hypoxic region. However, the sprouts move faster towards the hypoxic region, which keeps having a higher occupation fraction ϕ than in the case of physiological angiogenesis with lower r_J. Increasing Delta production decreases the number of sprouts (and thickens them), as corroborated by Ubezio *et al*'s experiments [46]. Fig. 11 depicts how the percentages of tip and stalk cells in moving sprouts evolve in time for the data of Fig. 10. In all cases, the percentages stabilize to the same low values of tip cells and high values of stalk cells after 2000 MCTS (time it takes the first sprouts to arrive at the hypoxic region). For shorter times, the influence of production rates on the relative number of tip/stalk cells is evident: higher r_J lowers the percentage of tip cells, whereas the influence of an increment of r_D on the percentage of tip/stalk cells is less clear. These data need to be contrasted with those of Figs. 5 to 7 to achieve a clearer picture of the morphology and thickness of the angiogenic network.

Results using case (B) dynamics with cell elongation . Numerical simulations with case (B) dynamics that includes cell elongation produce qualitatively the same results as reported in previous paragraphs. Obvious differences are that ECs are more elongated than in case (A) dynamics and that there is cell overtaking as shown in Fig. 2. Fig. 12 exhibits the elongated cells of case (B) dynamics when compared with the corresponding results of case (A) dynamics depicted in Fig. 5. Increasing the Jagged production rate gives rise to more vessel sprouts, and increasing the Delta-4 production rate decreases the number of tip cells and, consequently, decreases the number of sprouts; see Fig. 13.

Conclusion

The mathematical models of angiogenesis presented here illustrate the relative importance of mechanical, chemical and cellular cues when they are all considered simultaneously. Given a proliferation rate of cells and a VEGF gradient on a homogeneous extracellular matrix, competing J-N and D-N dynamics determine the influence of lateral inhibition and lateral induction on tip cell selection, branching, anastomosis and speed of angiogenesis. Anastomosis is driven by chemotaxis. Cellular motion is informed by haptotaxis and durotaxis. However, anastomosis may be favored or impeded depending on the mechanical configuration of strain vectors in the ECM near tip cells. Notch signaling determines tip cell selection and vessel branching. We consider tow types of cell dynamics. In case (A) dynamics, stalk cells are insensitive to chemical and mechanical cues and may be selected for proliferation when they are next to the tip cell of a growing sprout. Cellular division is informed by the local stress field. Tip cells can only proliferate once, when they start a new sprout, and move by sensing gradients of VEGF and stiffness. This dynamics tends to produce rounder stalk cells. In case (B) dynamics, cellular elongation is constrained and stalk cells move by also sensing chemical and mechanical cues but cellular chemotaxis is proportional to the ratio of the local Delta-4 concentration to the maximum possible value thereof. Thus, tip cells react more strongly to VEGF and are more motile than stalk cells. Yet, the latter also move and may overtake tip cells and replace them as the leading cell of a growing sprout.

For both case (A) and case (B) dynamics, lateral induction by stalk cells and lateral inhibition by tip cells are informed by competing Jagged-Notch and Delta-Notch dynamics in manners that depend quantitatively on the Delta and Jagged production rates. In particular, the numerical simulations of our model predict the following effects of the production rates. Increasing the production rate of Jagged favors lateral induction of stalk cells, which yields more hybrid tip/stalk cells and a thinner vasculature that advances faster. On the other hand and as observed in experiments [46], increasing the production rate of Delta lowers the number of tip cells by lateral inhibition of stalk cells. Then there are less sprouts and anastomosis is less frequent while the advance of the vascular plexus is only slightly faster. Our numerical simulations illustrate the regulating role of Notch-Jagged-Delta signaling in the velocity and morphology of angiogenic vasculature. An imbalance of the Jagged production, so that there is more Jagged and increased lateral induction of stalk cells, results in anomalous thinner sprouts and faster angiogenesis. This may be corrected by increasing the Delta-4 production rate, which boosts lateral inhibition of tip on stalk cells, diminishes the number of tips and slows down somewhat angiogenesis.

To allow for quantitative comparisons with experiments, e.g., [46], our 2D model of early stage angiogenesis needs to be extended in several directions to be made more realistic and to account for later stages of angiogenesis. The

extension of the model to three dimensional configurations is straightforward although it requires more computing power. While we have studied relatively short distances between the primary vessel and the target hypoxic region, we need to consider larger systems to be able to do statistical studies of vessel numbers and their width. To move toward later stages of the formation of an advancing vascular plexus, we need to add lumen formation [25] and blood circulation to the model [32]. These processes will allow us to tackle the concurrent sprouting and anastomosis on the front of the advancing vascular plexus and the pruning of poorly perfused sprouts on its back [32, 33].

Acknowledgements

This work resulted from a collaboration that began at the Workshop on Modeling Biological Phenomena from Nano to Macro Scales, held in 2018 at the Fields Institute in Toronto, Canada. We thank Prof. I. Hambleton, director of the Fields Institute, for the invitation and support during the Workshop, and also Prof. A. Carpio, the organizer of the Workshop. This work has been supported by the FEDER/Ministerio de Ciencia, Innovación y Universidades – Agencia Estatal de Investigación grant MTM2017-84446-C2-2-R (RV, MC and LLB). LLB thanks Russel Caflisch for hospitality during a sabbatical stay at the Courant Institute of Mathematical Sciences, New York University and acknowledges support of the Ministerio de Ciencia, Innovación y Universidades "Salvador de Madariaga" grant PRX18/00166. RDMT thanks the support of FEDER funds through the Operational Program Competitiveness Factors - COMPETE and by national funds by FCT - Foundation for Science and Technology under the strategic project UID/FIS/04564/2016 and under POCI-01-0145-FEDER-031743. RDMT acknowledges FCT's support through the FCT Researcher Program.

Supporting Information

S1 Text containing information on the numerical code. **S**2 Supporting movies with a README text file. All figures except for the schematic Fig. 3 have been extracted from numerical simulations of case (A) and case (B) dynamics and from snapshots from these and similar movies.

References

1. Folkman, J. (1995) Angiogenesis in cancer, vascular, rheumatoid and other disease. *Nature Medicine*, **1**, 27–30.
2. Carmeliet, P. (2005) Angiogenesis in life, disease and medicine. *Nature*, **438**, 932–936.
3. Tonnesen, M. G., Feng, X., and Clark, R. A. (2000) Angiogenesis in wound healing. *Journal of Investigative Dermatology Symposium Proceedings*, vol. 5, pp. 40–46, Elsevier.
4. Jackson, J. R., Seed, M., Kircher, C., Willoughby, D., and Winkler, J. (1997) The codependence of angiogenesis and chronic inflammation. *The FASEB Journal*, **11**, 457–465.
5. Carmeliet, P. (2003) Angiogenesis in health and disease. *Nature Medicine*, **9**, 653–660.
6. Folkman, J. (1971) Tumor angiogenesis: Therapeutic implications. *New England Journal of Medicine*, **285**, 1182–1186.
7. Liao, D. and Johnson, R. S. (2007) Hypoxia: a key regulator of angiogenesis in cancer. *Cancer and Metastasis Reviews*, **26**, 281–290.
8. Fidler, I. J. (2000) Angiogenesis and cancer metastasis. *Cancer Journal (Sudbury, Mass.)*, **6**, S134–41.
9. Carmeliet, P. and Jain, R. K. (2000) Angiogenesis in cancer and other diseases. *Nature*, **407**, 249–257.
10. Zuazo-Gaztelu, I. and Casanovas, O. (2018) Unraveling the role of angiogenesis in cancer ecosystems. *Frontiers in Oncology*, **8**, 248.

11. Maruotti, N., Cantatore, F., Crivellato, E., Vacca, A., and Ribatti, D. (2006) Angiogenesis in rheumatoid arthritis. *Histology and Histopathology*.

12. Jager, R. D., Mieler, W. F., and Miller, J. W. (2008) Age-related macular degeneration. *New England Journal of Medicine*, **358**, 2606–2617.

13. Taylor, R. N., Yu, J., Torres, P. B., Schickedanz, A. C., Park, J. K., Mueller, M. D., and Sidell, N. (2009) Mechanistic and therapeutic implications of angiogenesis in endometriosis. *Reproductive Sciences*, **16**, 140–146.

14. Laschke, M. and Menger, M. (2012) Anti-angiogenic treatment strategies for the therapy of endometriosis. *Human Reproduction Update*, **18**, 682–702.

15. Martin, A., Komada, M. R., and Sane, D. C. (2003) Abnormal angiogenesis in diabetes mellitus. *Medicinal Research Reviews*, **23**, 117–145.

16. Ferrara, N., Gerber, H.-P., and LeCouter, J. (2003) The biology of VEGF and its receptors. *Nature Medicine*, **9**, 669–676.

17. Chen, T. T., Luque, A., Lee, S., Anderson, S. M., Segura, T., and Iruela-Arispe, M. L. (2010) Anchorage of VEGF to the extracellular matrix conveys differential signaling responses to endothelial cells. *The Journal of Cell Biology*, **188**, 595–609.

18. Bentley, K., Gerhardt, H., and Bates, P. A. (2008) Agent-based simulation of notch-mediated tip cell selection in angiogenic sprout initialisation. *Journal of Theoretical Biology*, **250**, 25–36.

19. Gerhardt, H., et al. (2003) VEGF guides angiogenic sprouting utilizing endothelial tip cell filopodia. *The Journal of Cell Biology*, **161**, 1163–1177.

20. Hellstrom, M., et al. (2007) Dll4 signalling through Notch1 regulates formation of tip cells during angiogenesis. *Nature*, **445**, 776–780.

21. Meyer, G. T., Matthias, L. J., Noack, L., Vadas, M. A., and Gamble, J. R. (1997) Lumen formation during angiogenesis in vitro involves phagocytic activity, formation and secretion of vacuoles, cell death, and capillary tube remodelling by different populations of endothelial cells. *The Anatomical Record*, **249**, 327–340.

22. Lubarsky, B. and Krasnow, M. A. (2003) Tube morphogenesis: making and shaping biological tubes. *Cell*, **112**, 19–28.

23. Iruela-Arispe, M. L. and Davis, G. E. (2009) Cellular and molecular mechanisms of vascular lumen formation. *Developmental Cell*, **16**, 222–231.

24. Gebala, V., Collins, R., Geudens, I., Phng, L.-K., and Gerhardt, H. (2016) Blood flow drives lumen formation by inverse membrane blebbing during angiogenesis in vivo. *Nature Cell Biology*, **18**, 443–450.

25. Boas, S. E. and Merks, R. M. H. (2014) Synergy of cell–cell repulsion and vacuolation in a computational model of lumen formation. *Journal of The Royal Society Interface*, **11**, 20131049.

26. Moreira-Soares, M., Coimbra, R., Rebelo, L., Carvalho, J., and Travasso, R. D. M. (2018) Angiogenic factors produced by hypoxic cells are a leading driver of anastomoses in sprouting angiogenesis–a computational study. *Scientific reports*, **8**, 8726.

27. Fantin, A., Vieira, J. M., Gestri, G., Denti, L., Schwarz, Q., Prykhozhij, S., Peri, F., Wilson, S. W., and Ruhrberg, C. (2010) Tissue macrophages act as cellular chaperones for vascular anastomosis downstream of VEGF-mediated endothelial tip cell induction. *Blood*, **116**, 829–840.

28. Zhan, K., Bai, L., and Xu, J. (2013) Role of vascular endothelial progenitor cells in construction of new vascular loop. *Microvascular Research*, **90**, 1–11.

29. Geudens, I. and Gerhardt, H. (2011) Coordinating cell behaviour during blood vessel formation. *Development*, **138**, 4569–4583.

30. Flores, J., Romero, A. M., Travasso, R. D. M., and Poiré, E. C. (2013) Flow and anastomosis in vascular networks. *Journal of Theoretical Biology*, **317**, 257–270.

31. Franco, C. A., et al. (2015) Dynamic endothelial cell rearrangements drive developmental vessel regression. *PLoS Biology*, **13**, e1002125.

32. Bernabeu, M. O., Jones, M. L., Nash, R. W., Pezzarossa, A., Coveney, P. V., Gerhardt, H., and Franco, C. A. (2018) PolNet: A tool to quantify network-level cell polarity and blood flow in vascular remodeling. *Biophysical Journal*, **114**, 2052–2058.

33. Szymborska, A. and Gerhardt, H. (2018) Hold me, but not too tight - endothelial cell-cell junctions in angiogenesis. *Cold Spring Harb. Perspect. Biol.*, **10**, a029223.

34. Lobov, I., Renard, R., Papadopoulos, N., Gale, N., Thurston, G., Yancopoulos, G., and Wiegand, S. (2007) Delta-like ligand 4 (Dll4) is induced by VEGF as a negative regulator of angiogenic sprouting. *Proceedings of the National Academy of Sciences*, **104**, 3219–3224.

35. Phng, L.-K. and Gerhardt, H. (2009) Angiogenesis: a team effort coordinated by Notch. *Developmental Cell*, **16**, 196–208.

36. Santos-Oliveira, P., Correia, A., Rodrigues, T., Ribeiro-Rodrigues, T. M., Matafome, P., Rodríguez-Manzaneque, J. C., Seiça, R., Girão, H., and Travasso, R. D. M. (2015) The force at the tip - modelling tension and proliferation in sprouting angiogenesis. *PLoS Computational Biology*, **11**, e1004436.

37. Jakobsson, L., et al. (2010) Endothelial cells dynamically compete for the tip cell position during angiogenic sprouting. *Nature Cell Biology*, **12**, 943–953.

38. Arima, S., Nishiyama, K., Ko, T., Arima, Y., Hakozaki, Y., Sugihara, K., Koseki, H., Uchijima, Y., Kurihara, Y., and Kurihara, H. (2011) Angiogenic morphogenesis driven by dynamic and heterogeneous collective endothelial cell movement. *Development*, **138**, 4763–4776.

39. Cruys, B., et al. (2016) Glycolytic regulation of cell rearrangement in angiogenesis. *Nature Communications*, **7**, 12240.

40. Cantelmo, A. R., et al. (2016) Inhibition of the glycolytic activator PFKFB3 in endothelium induces tumor vessel normalization, impairs metastasis, and improves chemotherapy. *Cancer Cell*, **30**, 968–985.

41. Conradi, L.-C., et al. (2017) Tumor vessel disintegration by maximum tolerable PFKFB3 blockade. *Angiogenesis*, **20**, 599–613.

42. Cantelmo, A. R., Pircher, A., Kalucka, J., and Carmeliet, P. (2017) Vessel pruning or healing: endothelial metabolism as a novel target? *Expert Opinion on Therapeutic Targets*, **21**, 239–247.

43. Eilken, H. M. and Adams, R. H. (2010) Dynamics of endothelial cell behavior in sprouting angiogenesis. *Current Opinion in Cell Biology*, **22**, 617–625.

44. Bentley, K., et al. (2014) The role of differential VE-cadherin dynamics in cell rearrangement during angiogenesis. *Nature Cell Biology*, **16**, 309.

45. Warren, C. M. and Iruela-Arispe, M. L. (2010) Signaling circuitry in vascular morphogenesis. *Current Opinion in Hematology*, **17**, 213.

46. Ubezio, B., Blanco, R. A., Geudens, I., Stanchi, F., Mathivet, T., Jones, M. L., Ragab, A., Bentley, K., and Gerhardt, H. (2016) Synchronization of endothelial Dll4-Notch dynamics switch blood vessels from branching to expansion. *Elife*, **5**, e12167.

47. Venkatraman, L., Regan, E. R., and Bentley, K. (2016) Time to decide? dynamical analysis predicts partial tip/stalk patterning states arise during angiogenesis. *PloS ONE*, **11**, e0166489.

48. Boareto, M., Jolly, M. K., Ben-Jacob, E., and Onuchic, J. N. (2015) Jagged mediates differences in normal and tumor angiogenesis by affecting tip-stalk fate decision. *Proceedings of the National Academy of Sciences*, **112**, E3836–E3844.

49. Boareto, M., Jolly, M. K., Lu, M., Onuchic, J. N., Clementi, C., and Ben-Jacob, E. (2015) Jagged–Delta asymmetry in notch signaling can give rise to a sender/receiver hybrid phenotype. *Proceedings of the National Academy of Sciences*, **112**, E402–E409.

50. Boareto, M., Jolly, M. K., Goldman, A., Pietilä, M., Mani, S. A., Sengupta, S., Ben-Jacob, E., Levine, H., and Onuchic, J. N. (2016) Notch-Jagged signalling can give rise to clusters of cells exhibiting a hybrid epithelial/mesenchymal phenotype. *Journal of the Royal Society Interface*, **13**, 20151106.

51. Jolly, M. K., Boareto, M., Lu, M., Onuchic, J. N., Clementi, C., and Ben-Jacob, E. (2015) Operating principles of Notch–Delta–Jagged module of cell–cell communication. *New Journal of Physics*, **17**, 055021.

52. Benedito, R., Roca, C., Sörensen, I., Adams, S., Gossler, A., Fruttiger, M., and Adams, R. H. (2009) The notch ligands Dll4 and Jagged1 have opposing effects on angiogenesis. *Cell*, **137**, 1124–1135.

53. Hofmann, J. J. and Iruela-Arispe, M. L. (2007) Notch expression patterns in the retina: an eye on receptor–ligand distribution during angiogenesis. *Gene Expression Patterns*, **7**, 461–470.

54. Sjöqvist, M. and Andersson, E. R. (2017) Do as i say, not (ch) as i do: Lateral control of cell fate. *Developmental biology*.

55. Orme, M. E. and Chaplain, M. A. J. (1996) A mathematical model of vascular tumour growth and invasion. *Mathl. Comput. Modelling*, **23**, 43–60.

56. Orme, M. E. and Chaplain, M. A. J. (1997) Two-dimensional models of tumour angiogenesis and anti-angiogenesis strategies. *Mathematical Medicine and Biology*, **14**, 189–205.

57. Levine, H. A., Sleeman, B. D., and Nilsen-Hamilton, M. (2000) A mathematical model for the roles of pericytes and macrophages in the initiation of angiogenesis. i. the role of protease inhibitors in preventing angiogenesis. *Mathematical Biosciences*, **168**, 77–115.

58. Levine, H. A., Pamuk, S., Sleeman, B. D., and Nilsen-Hamilton, M. (2001) Mathematical modeling of capillary formation and development in tumor angiogenesis: penetration into the stroma. *Bulletin of Mathematical Biology*, **63**, 801–863.

59. Plank, M., Sleeman, B., and Jones, P. (2004) The role of the angiopoietins in tumour angiogenesis. *Growth Factors*, **22**, 1–11.

60. Stokes, C. L. and Lauffenburger, D. A. (1991) Analysis of the roles of microvessel endothelial cell random motility and chemotaxis in angiogenesis. *Journal of Theoretical Biology*, **152**, 377–403.

61. Anderson, A. R. and Chaplain, M. (1998) Continuous and discrete mathematical models of tumor-induced angiogenesis. *Bulletin of Mathematical Biology*, **60**, 857–899.

62. McDougall, S. R., Anderson, A., Chaplain, M., and Sherratt, J. (2002) Mathematical modelling of flow through vascular networks: implications for tumour-induced angiogenesis and chemotherapy strategies. *Bulletin of Mathematical Biology*, **64**, 673–702.

63. Mantzaris, N. V., Webb, S., and Othmer, H. G. (2004) Mathematical modeling of tumor-induced angiogenesis. *Journal of Mathematical Biology*, **49**, 111–187.

64. Macklin, P., McDougall, S., Anderson, A. R., Chaplain, M. A., Cristini, V., and Lowengrub, J. (2009) Multiscale modelling and nonlinear simulation of vascular tumour growth. *Journal of Mathematical Biology*, **58**, 765–798.

65. Perfahl, H., et al. (2011) Multiscale modelling of vascular tumour growth in 3d: the roles of domain size and boundary conditions. *PloS ONE*, **6**, e14790.

66. Merks, R. M. H., Perryn, E. D., Shirinifard, A., and Glazier, J. A. (2008) Contact-inhibited chemotaxis in de novo and sprouting blood-vessel growth. *PLoS Computational Biology*, **4**, e1000163.

67. van Oers, R. F. M., Rens, E. G., LaValley, D. J., Reinhart-King, C. A., and Merks, R. M. H. (2014) Mechanical cell-matrix feedback explains pairwise and collective endothelial cell behavior in vitro. *PLOS Computational Biology*, **10**, 1–14.

68. Heck, T., Vaeyens, M., and Van Oosterwyck, H. (2015) Computational models of sprouting angiogenesis and cell migration: towards multiscale mechanochemical models of angiogenesis. *Mathematical Modelling of Natural Phenomena*, **10**, 108–141.

69. Travasso, R. D. M., Castro, M., and Oliveira, J. C. R. E. (2011) The phase-field model in tumor growth. *Philosophical Magazine*, **91**, 183–206.

70. Travasso, R. D. M., Corvera Poiré, E., Castro, M., Rodríguez-Manzaneque, J. C., and Hernández-Machado, A. (2011) Tumor angiogenesis and vascular patterning: A mathematical model. *PLoS ONE*, **6**, e19989.

71. Bonilla, L. L., Capasso, V., Alvaro, M., and Carretero, M. (2014) Hybrid modeling of tumor-induced angiogenesis. *Physical Review E*, **90**, 062716.

72. Terragni, F., Carretero, M., Capasso, V., and Bonilla, L. L. (2016) Stochastic model of tumor-induced angiogenesis: Ensemble averages and deterministic equations. *Physical Review E*, **93**, 022413.

73. Bonilla, L. L., Carretero, M., and Terragni, F. (2016) Solitonlike attractor for blood vessel tip density in angiogenesis. *Physical Review E*, **94**, 062415.

74. Lakatos, D., Somfai, E., Méhes, E., and Czirók, A. (2018) Soluble VEGFR1 signaling guides vascular patterns into dense branching morphologies. *Journal of Theoretical Biology*.

75. Graner, F. and Glazier, J. A. (1992) Simulation of biological cell sorting using a two-dimensional extended Potts model. *Physical Review Letters*, **69**, 2013–2016.

76. Chen, N., Glazier, J. A., Izaguirre, J. A., and Alber, M. S. (2007) A parallel implementation of the Cellular Potts model for simulation of cell-based morphogenesis. *Computer Physics Communications*, **176**, 670–681.

77. Bauer, A. L., Jackson, T. L., and Jiang, Y. (2007) A cell-based model exhibiting branching and anastomosis during tumor-induced angiogenesis. *Biophysical Journal*, **92**, 3105–3121.

78. Shirinifard, A., Gens, J. S., Zaitlen, B. L., Popławski, N. J., Swat, M., and Glazier, J. A. (2009) 3d multi-cell simulation of tumor growth and angiogenesis. *PloS ONE*, **4**, e7190.

79. Bauer, A. L., Jackson, T. L., and Jiang, Y. (2009) Topography of extracellular matrix mediates vascular morphogenesis and migration speeds in angiogenesis. *PLoS Computational Biology*, **5**, e1000445.

80. Shamloo, A., Mohammadaliha, N., Heilshorn, S. C., and Bauer, A. L. (2016) A comparative study of collagen matrix density effect on endothelial sprout formation using experimental and computational approaches. *Annals of Biomedical Engineering*, **44**, 929–941.

81. Ramos, J. R. D., Travasso, R. D. M., and Carvalho, J. (2018) Capillary network formation from dispersed endothelial cells: influence of cell traction, cell adhesion and extracellular matrix rigidity. *Physical Review E*, **97**, 012408.

82. Bentley, K., Mariggi, G., Gerhardt, H., and Bates, P. A. (2009) Tipping the balance: Robustness of tip cell selection, migration and fusion in angiogenesis. *PLoS Computational Biology*, **5**, e1000549.

83. Landau, L. D. and Lifshitz, E. M. (1976) *Mechanics. 3rd ed*. Pergamon Press New York.

84. Merks, R. M. H., Brodsky, S. V., Goligorksy, M. S., Newman, S. A., and Glazier, J. A. (2006) Cell elongation is key to in silico replication of in vitro vasculogenesis and subsequent remodeling. *Developmental Biology*, **289**, 44–54.

85. Sugihara, K., et al. (2015) Autonomy and non-autonomy of angiogenic cell movements revealed by experiment-driven mathematical modeling. *Cell Reports*, **13**, 1814–1827.

86. Boas, S. E. and Merks, R. M. H. (2015) Tip cell overtaking occurs as a side effect of sprouting in computational models of angiogenesis. *BMC Systems Biology*, **9**, 86.

87. Herz, K., Becker, A., Shi, C., Ema, M., Takahashi, S., Potente, M., Hesse, M., Fleischmann, B. K., and Wenzel, D. (2018) Visualization of endothelial cell cycle dynamics in mouse using the Flt-1/eGFP-anillin system. *Angiogenesis*, **21**, 349–361.

88. Markovtsev, V. and Cuadros, M. (2017), Src–d/kmcuda: 6.0.0–1.

89. Reinhart-King, C. A., Dembo, M., and Hammer, D. A. (2008) Cell-cell mechanical communication through compliant substrates. *Biophysical Journal*, **95**, 6044–6051.

90. Kohn, J. C., Zhou, D. W., Bordeleau, F., Zhou, A. L., Mason, B. N., Mitchell, M. J., King, M. R., and Reinhart-King, C. A. (2015) Cooperative effects of matrix stiffness and fluid shear stress on endothelial cell behavior. *Biophysical Journal*, **108**, 471–478.

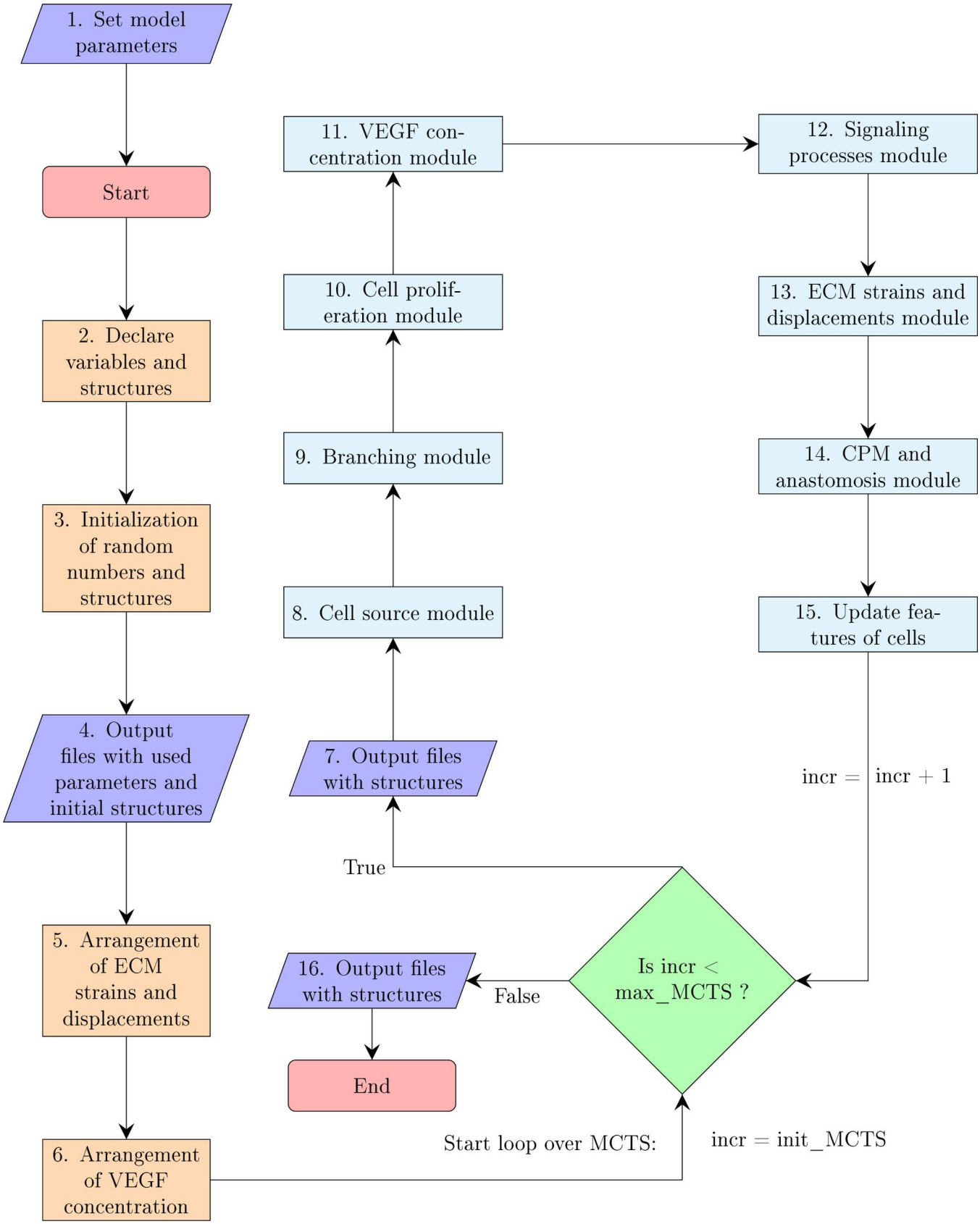

Figure 3. Flow diagram of the simulation model.

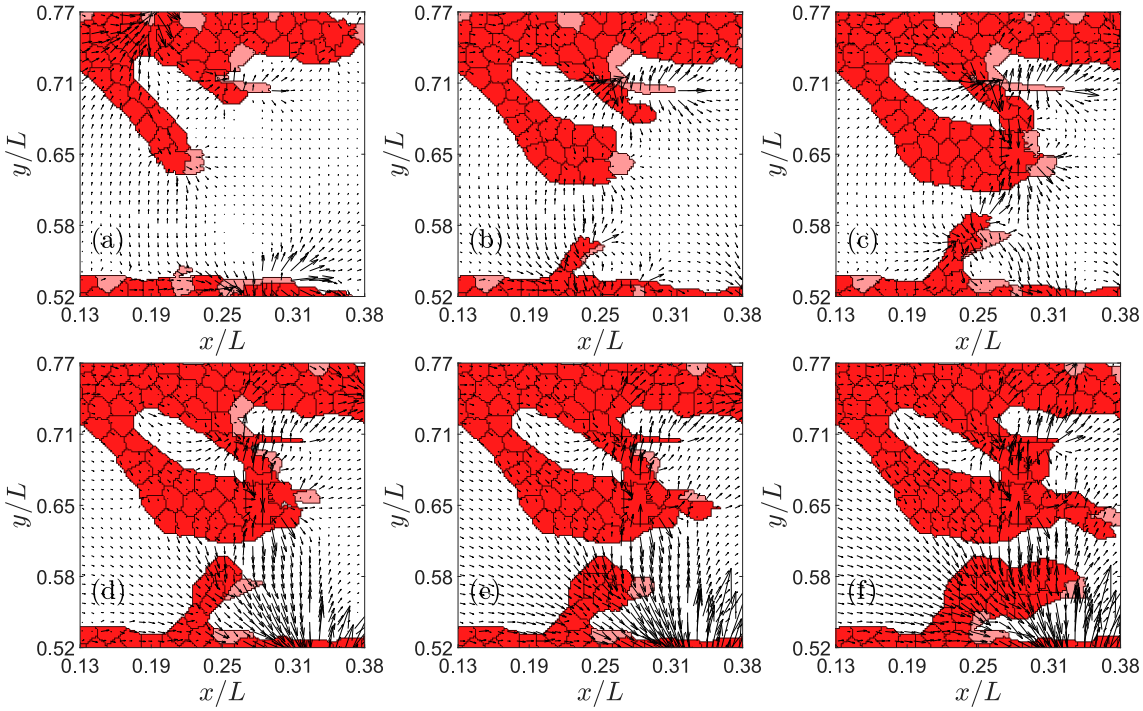

Figure 4. Example of successful and frustrated anastomosis. Times in MCTS are: (a) 751, (b) 851, (c) 951, (d) 1051, (e) 1101, (f) 1201. Tip cells are pink.

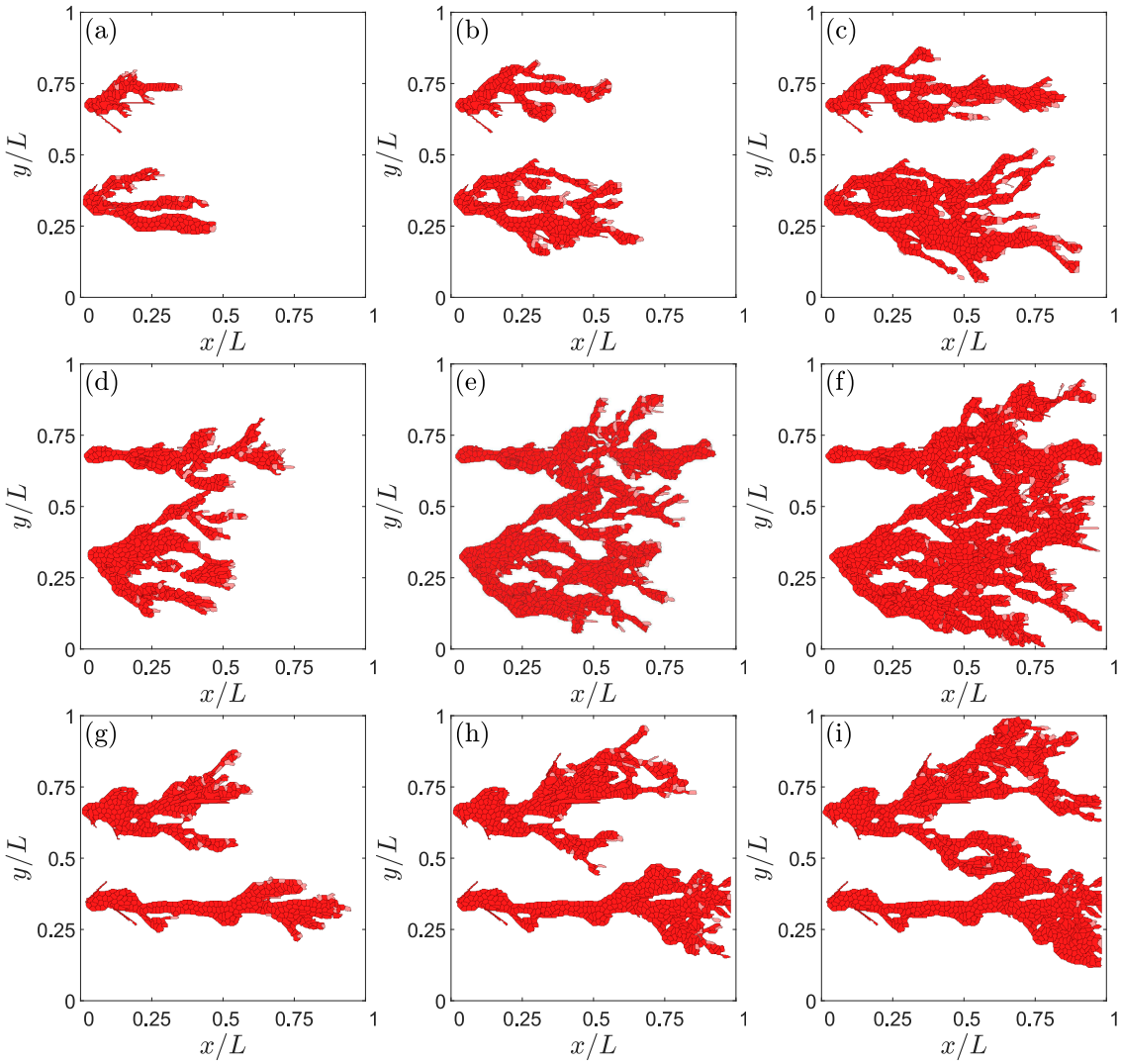

Figure 5. Effect of Jagged production on angiogenesis. For $r_J = 500$ molec/h and $r_D = 1000$ molec/h, snapshots at times: (a) 2001 MCTS, (b) 2751 MCTS, (c) 3501 MCTS. For $r_J = 2000$ molec/h and $r_D = 1000$ molec/h, snapshots at times: (d) 2001 MCTS, (e) 2751 MCTS, (f) 3501 MCTS. For $r_J = 2000$ molec/h and $r_D = 7500$ molec/h, snapshots at times: (g) 2001 MCTS, (h) 2501 MCTS, (i) 3501 MCTS.

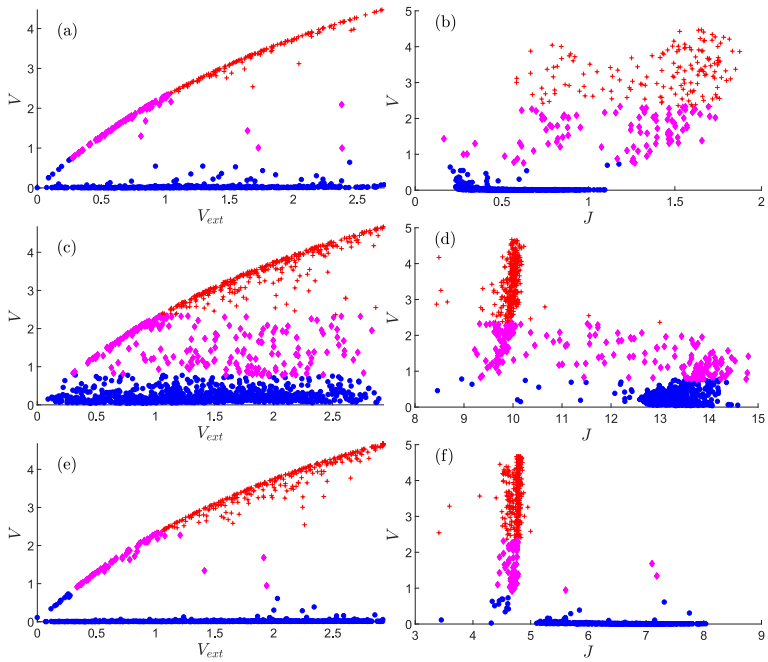

Figure 6. Content of VEGF, V, versus $V_{\text{ext}} = C$, and of V versus J in the tip, stalk and hybrid tip-stalk cells within the angiogenic network at 3501 MCTS. (a), (b) $r_J = 500$ molec/h, $r_D = 1000$ molec/h; (c), (d) $r_J = 2000$ molec/h, $r_D = 1000$ molec/h; (e), (f): $r_J = 2000$ molec/h, $r_D = 7500$ molec/h. Other parameter values are as indicated in Tables 1-3. Nondimensional units for V, V_{ext}, J are as indicated in Table 4. The meaning of symbols is as follows. Red cross (tip cell), magenta rhombus (hybrid tip/stalk cell), blue circle (stalk cell).

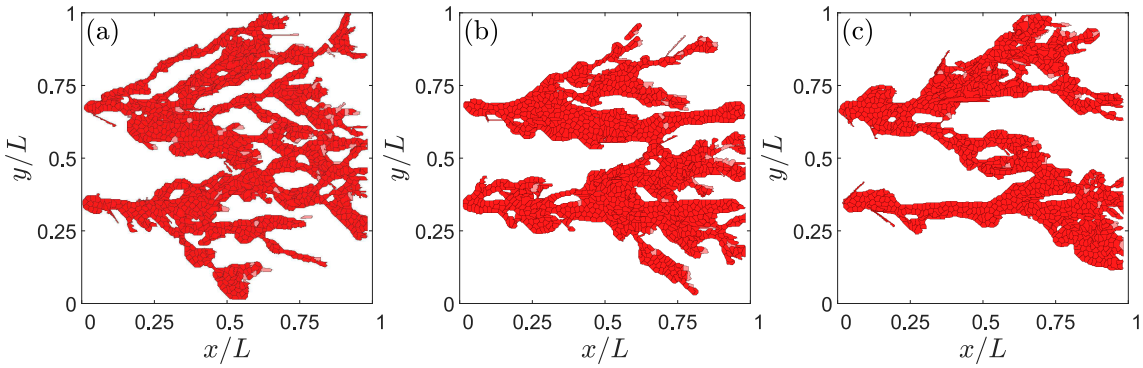

Figure 7. Effect of the Delta production rate on angiogenesis with a high Jagged production rate of $r_J = 2000$ **molec/h at 3501 MCTS.** (a) $r_D = 3000$ molec/h, (b) $r_D = 6000$ molec/h, and (c) $r_D = 7500$ molec/h. Lateral inhibition due to more activated D-N signaling decreases the number of hybrid tip/stalk cells and branching.

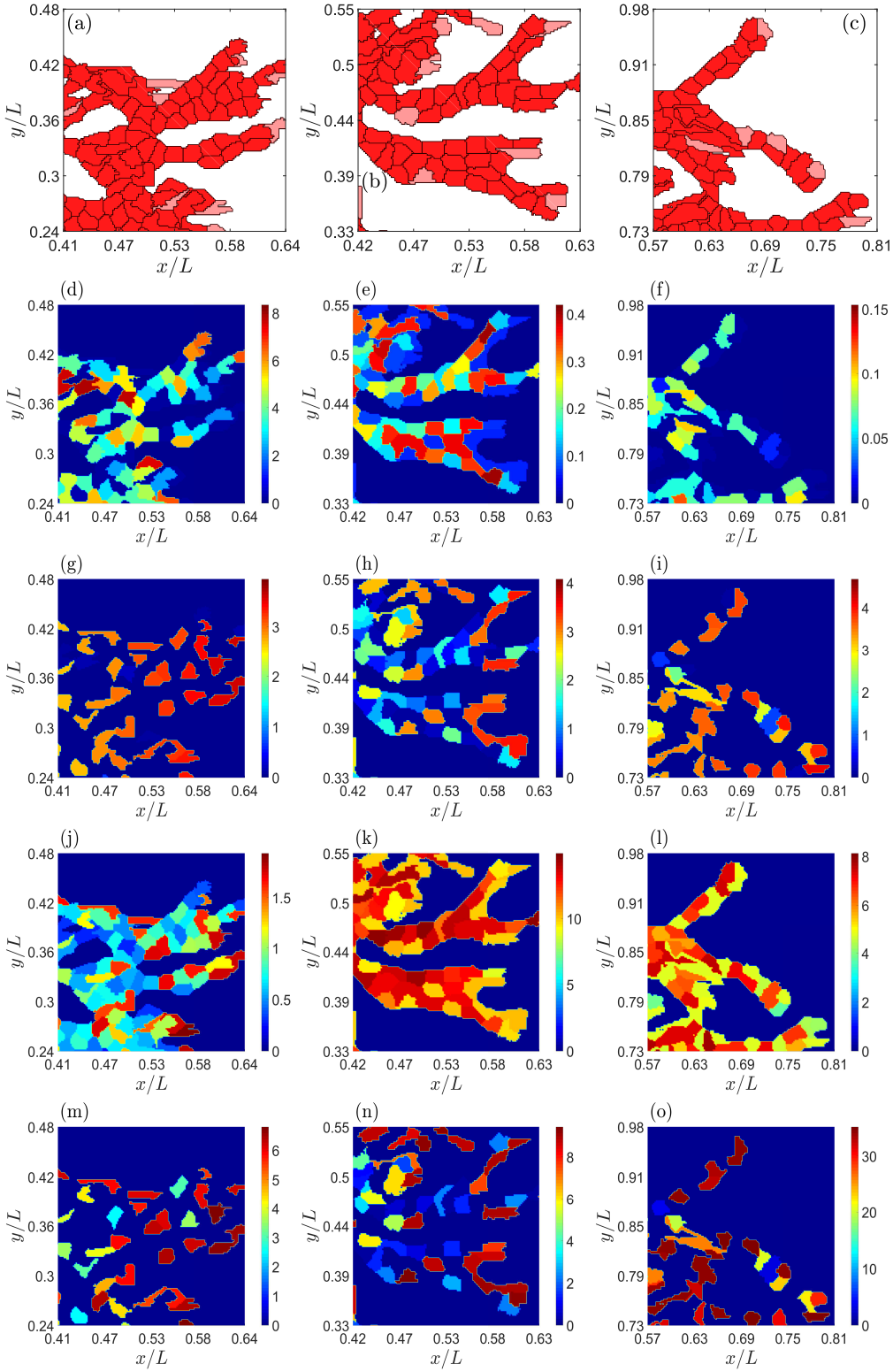

Figure 8. Effect of the Jagged and Delta production rates on angiogenesis at a time of 2901 MCTS. (a)-(c) Snapshots of networks, (d)-(f) Notch concentration, (g)-(i) VEGF concentration, (j)-(l) Jagged-1 concentration, (m)-(o) Delta-4 concentration. Data: (a),(d),(g),(j),(m) $r_J = 500$ molec/h, $r_D = 1000$ molec/h, (b),(e),(h),(k),(n): $r_J = 2000$ molec/h, $r_D = 1000$ molec/h, (c),(f),(i),(l),(o): $r_J = 2000$ molec/h, $r_D = 7500$ molec/h. Nondimensional units for protein concentrations are as in Table 4.

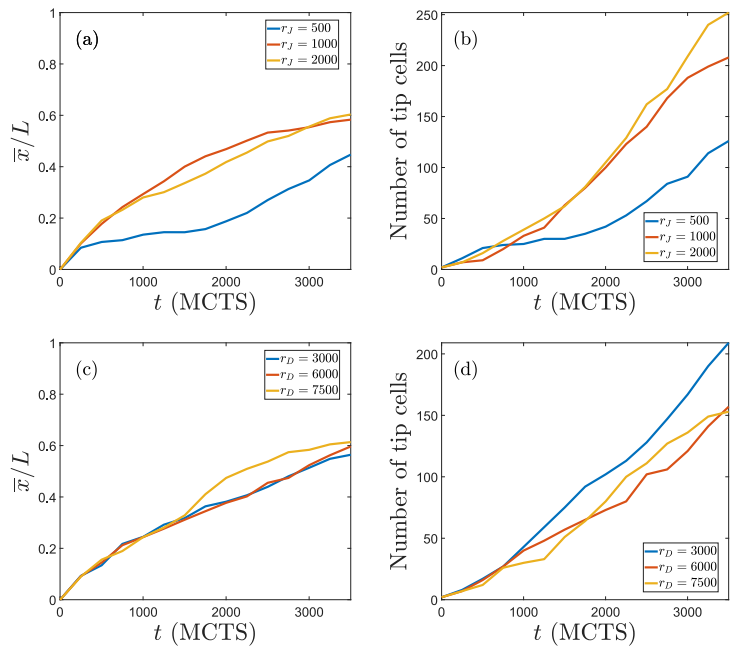

Figure 9. Effect of varying the production rates of Jagged and Delta on the advance and morphology of the vascular plexus. (a) Average abscissa (position on x axis) of the tip cells as a function of time, and (b) number of tip cells versus time for $r_D = 1000$ molec/h and $r_J = 500$, 1000 and 2000 molec/h. Increasing Jagged production rate yields more tip cells that advance faster. (c) Average position of tip cells versus time, and (d) number of tip cells versus time, for $r_J = 2000$ molec/h and $r_D = 3000$, 6000 and 7500 molec/h. Increasing Delta production rate makes tip cells to advance slightly more but it diminishes the number of tip cells. The effect of r_D on the number of tip cells is opposite to that of r_J in Panels (a) and (b).

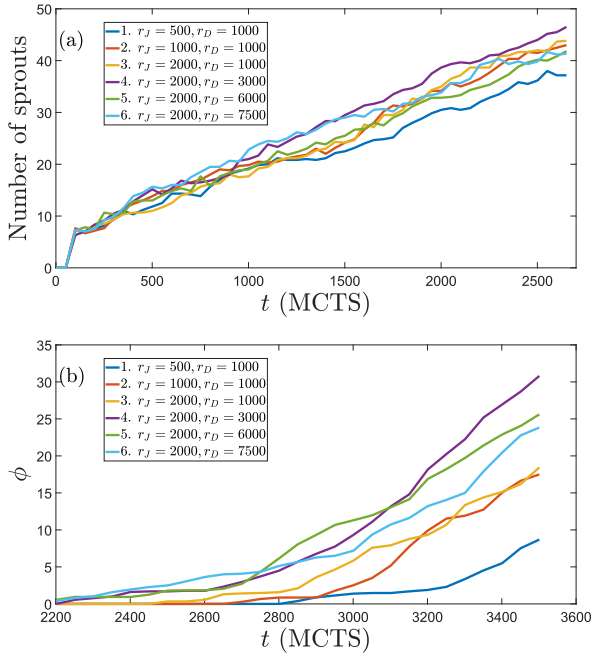

Figure 10. Sensitivity of simulation results to changes in the parameters controlling cellular signaling. (a) Number of angiogenic sprouts versus time, and (b) percentage of pixels ϕ at $x = L$ (the hypoxic region) that are occupied by vessel sprouts versus time, for the indicated Jagged and Delta production rates. Data correspond to averages over 6 realizations of the stochastic process.

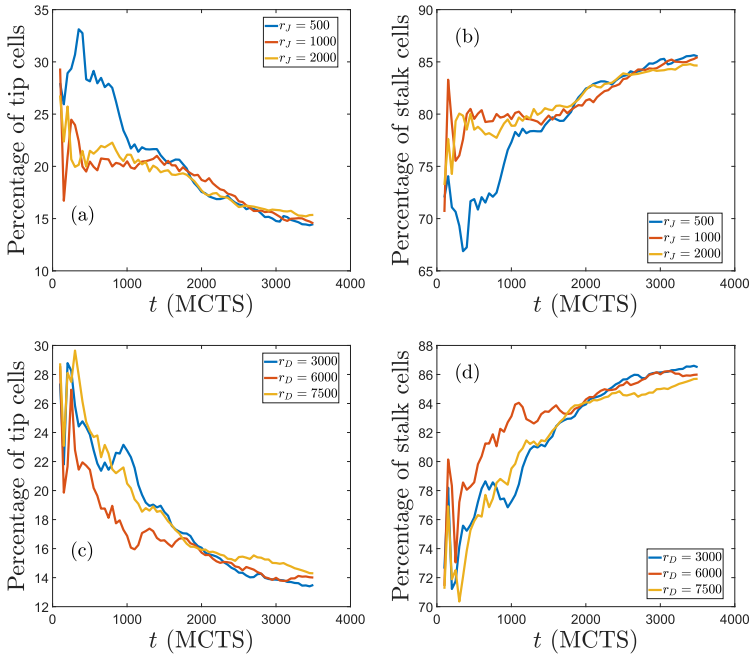

Figure 11. Percentage of tip and stalk cells versus time for the simulations displayed in Fig. 10. Production rates are $r_D = 1000$ molec/h in panels (a) and (b), and $r_J = 2000$ molec/h in panels (c) and (d).

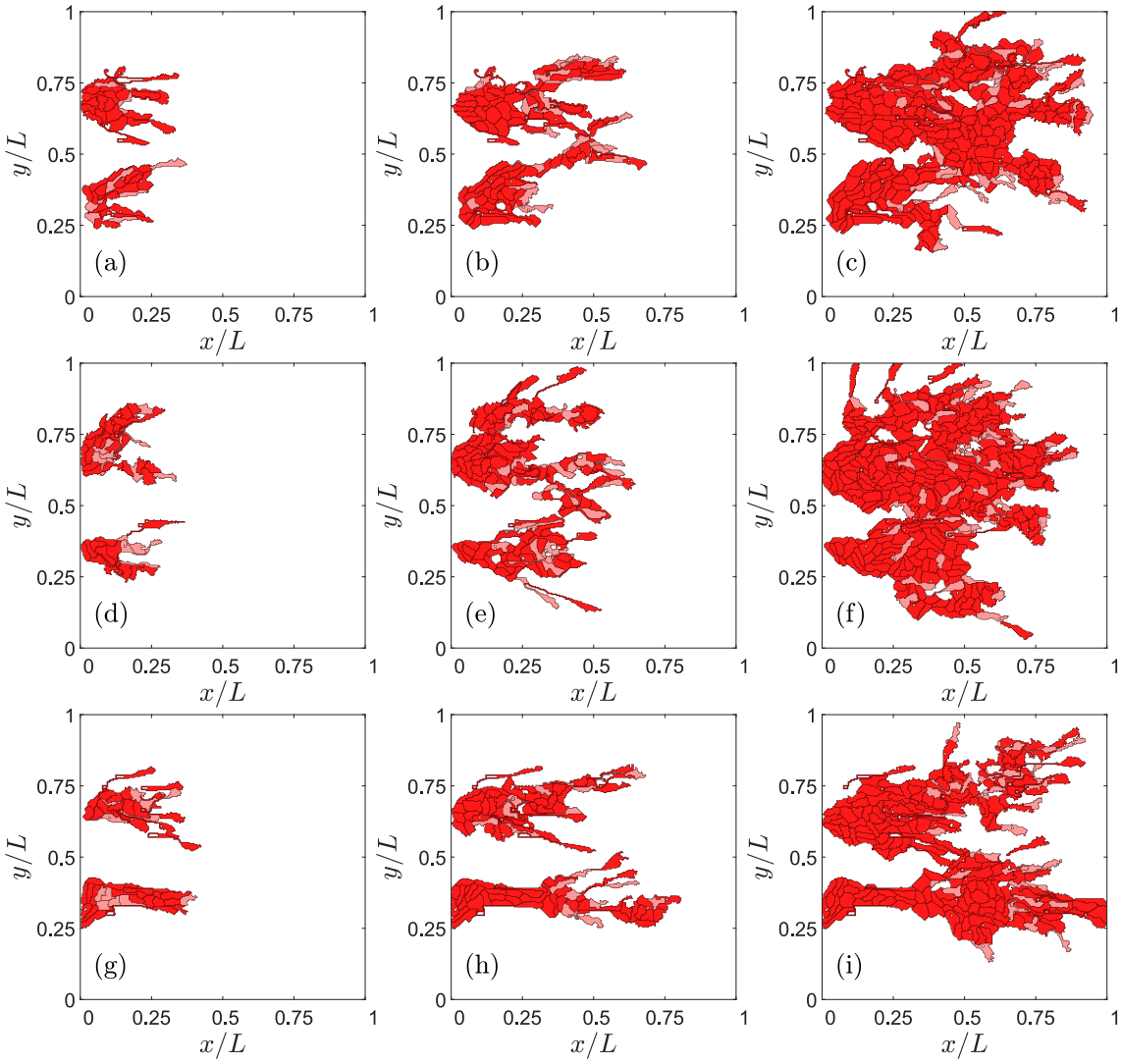

Figure 12. Effect of Jagged production on angiogenesis for case (B) elongational cellular dynamics and a sample of half length than for case (A) dynamics. For $r_J = 500$ molec/h and $r_D = 1000$ molec/h, snapshots at times: (a) 801 MCTS, (b) 1601 MCTS, (c) 2401 MCTS. For $r_J = 2000$ molec/h and $r_D = 1000$ molec/h, snapshots at times: (d) 801 MCTS, (e) 1601 MCTS, (f) 2401 MCTS. For $r_J = 2000$ molec/h and $r_D = 7500$ molec/h, snapshots at times: (g) 801 MCTS, (h) 1601 MCTS, (i) 2401 MCTS.

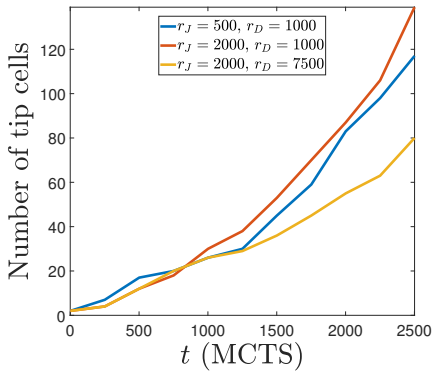

Figure 13. Number of tip cells versus time for $r_J = 500$ and 2000 molec/h, $r_D = 1000$ and 7500 molec/h with the elongational cell dynamics of case (B).